Rock Mechanics and Rock Engineering (2023) 56:2065–2101
https://doi.org/10.1007/s00603-022-03129-7

ORIGINAL PAPER

Strain Partitioning and Frictional Behavior of Opalinus Clay During Fault Reactivation

Valerian Schuster[1,2] · Erik Rybacki[1] · Audrey Bonnelye[1,3] · Grzegorz Kwiatek[1] · Anja M. Schleicher[1,2] · Georg Dresen[1,2]

Received: 15 March 2022 / Accepted: 25 October 2022 / Published online: 30 November 2022

Abstract

The Opalinus Clay (OPA) formation is considered a suitable host rock candidate for nuclear waste storage. However, the sealing integrity and long-term safety of OPA are potentially compromised by pre-existing natural or artificially induced faults. Therefore, characterizing the mechanical behavior and microscale deformation mechanisms of faults and the surrounding rock is relevant for predicting repository damage evolution. In this study, we performed triaxial tests using saw-cut samples of the shaly and sandy facies of OPA to investigate the influence of pressure and mineral composition on the deformation behavior during fault reactivation. Dried samples were hydrostatically pre-compacted at 50 MPa and then deformed at constant strain rate, drained conditions and confining pressures (p_c) of 5–35 MPa. Mechanical data from triaxial tests was complemented by local strain measurements to determine the relative contribution of bulk deformation and fault slip, as well as by acoustic emission (AE) monitoring, and elastic P-wave velocity measurements using ultrasonic transmissions. With increasing p_c, we observe a transition from brittle deformation behavior with highly localized fault slip to semi-brittle behavior characterized by non-linear strain hardening with increasing delocalization of deformation. We find that brittle localization behavior is limited by p_c at which fault strength exceeds matrix yield strength. AEs were only detected in tests performed on sandy facies samples, and activity decreased with increasing p_c. Microstructural analysis of deformed samples revealed a positive correlation between increasing p_c and gouge layer thickness. This goes along with a change from brittle fragmentation and frictional sliding to the development of shear zones with a higher contribution of cataclastic and granular flow. Friction coefficient at fault reactivation is only slightly higher for the sandy ($\mu \sim 0.48$) compared to the shaly facies ($\mu \sim 0.4$). Slide-hold-slide tests performed after ~ 6 mm axial shortening suggest stable creeping and long-term weakness of faults at the applied conditions. Our results demonstrate that the mode of fault reactivation highly depends on the present stress field and burial history.

✉ Valerian Schuster
valerian.schuster@gfz-potsdam.de

[1] Helmholtz Centre Potsdam, GFZ German Research Centre for Geosciences, 14473 Potsdam, Germany

[2] Institute for Earth and Environmental Science, University of Potsdam, 14476 Potsdam, Germany

[3] Department of Earth Sciences, Free University Berlin, 12249 Berlin, Germany

Highlights

- Fault slip behavior of sandy and shaly facies samples of Opalinus Clay is highly pressure sensitive.
- Brittle localization behavior is limited to the confining pressures at which fault strength exceeds matrix yield strength.
- With increasing confining pressure, gouge layer width increases and anastomosing shear plane networks develop during shear dominated by cataclastic (sandy facies) and granular (shaly facies) flow.
- Restrengthening of shaly and sandy facies Opalinus Clay is minor.

Keywords Opalinus Clay · Triaxial deformation · Strain partitioning · Fault reactivation · Microstructures

List of Symbols

μ	Amonton's friction coefficient
L	Sample length
θ	Angle between saw-cut plane and samples axis
S_q	Root mean square (RMS) roughness
ρ	Bulk density
φ	Porosity
p_c	Confining pressure
D_{tot}	Total axial shortening of the specimen
D_{LVDT}	Piston (LVDT) displacement
ε_{tot}	Total axial strain
ε_{ax}	Axial matrix strain
s_f	Slip along the saw-cut plane
ε_{vol}	Volumetric matrix strain
σ_1	Maximum principal stress
τ	Shear stress
σ_n	Normal stress
t_h	Hold period
$\Delta\mu_c$	Creep relaxation
$\Delta\mu_h$	Frictional strengthening
$\Delta\mu_w$	Frictional weakening
d_w	Slip weakening distance
σ_d	Differential stress
σ_y	Yield stress bulk matrix
σ_f	Stress at onset of fault slip
ε_{rad}	Radial matrix strain
v_{sf}	Slip rate along the saw-cut plane
ε_{tf}	Transformed fault-parallel strain
$\sigma^H{}_d$	Differential stress at the start of Slide-Hold-Slide tests
β_c	Creep relaxation rate
β_h	Frictional healing rate
p	Mean effective pressure
v	Specific volume
μ_f	Friction coefficient at onset of fault slip
k_m	Compliance of the testing machine
$\dot{\varepsilon}_s$	Specimen relaxation strain rate
σ_{ci}	Uniaxial compressive strength (UCS)
ϕ	Friction angle
c	Cohesion
m_i	Material-specific constant
σ_{matrix}	Matrix failure/flow strength
k_s	Specimen compliance
l_m	Conversion factor
$\dot{\varepsilon}_{creep}$	Creep strain rate
n	Power-law stress exponent
β	Exponential law stress gradient
$\frac{d\sigma}{dt}$	Stress rate

1 Introduction

Characterized by a low hydraulic permeability (10^{-19}–10^{-21} m^2), high self-sealing potential as well as sorption and retention capacity, the Opalinus Clay (OPA) formation has been selected as a suitable host rock for deep geological storage of nuclear waste in Switzerland (NAGRA 2002; Bossart and Milnes 2017). At any future repository site, the host rock is required to maintain integrity as a geological barrier over long time scales. However, the presence of pre-existing natural fractures and faults will alter the mechanical and hydraulic properties of the formation, thereby compromising its sealing capacity (Tsang et al. 2012). During the construction and lifetime of a repository, structural discontinuities can destabilize by changes in the effective stress field and may potentially trigger seismic hazard and damage to underground facilities. In the context of deep geological storage of nuclear waste, changes in the stress field may be induced by construction measures (e.g., tunneling activity) that can lead to the failure of the intact rock and/or to reactivation of bedding planes and faults (Lisjak et al. 2015; Amann et al. 2018; Rinaldi and Urpi 2020; Hopp et al. 2022). Furthermore, the alteration of in-situ pore pressure can change the effective stress state. After waste emplacement, nuclear decay processes will generate heat that can lead to the formation of excess pore pressure caused by the thermally induced expansion of the pore fluid in the low-permeable host rock (thermal pressurization; e.g., Gens et al. 2007; Ghabezloo and Sulem 2009; Urpi et al. 2019). Gas formation due to anaerobic microbial corrosion of emplaced steel canisters (Ortiz et al. 2002) as well as dynamic strains induced by natural distant earthquakes (Barbour 2015) can also locally change

pore pressure. With increasing pore pressure, the effective normal stress acting on fault planes will decrease, which can lead to fault reactivation if the shear stress resolved on the fault plane exceeds the shear strength. Reactivation of faults may not only result in seismicity but can also lead to the creation of permeable fluid flow paths along faults and fractures. These may provide an opportunity for the release and migration of radioactive nuclides if they remain hydraulically conductive. Therefore, an important aspect of the long-term safety of future repository sites is the risk assessment for fault activation caused by stress perturbations.

Tectonic structures in OPA and other clay-rich host rocks may be detected by in-situ geophysical methods (e.g., Jaeggi et al. 2017; Schuster et al. 2017). However, on a regional scale, a resolution is limited due to a low impedance contrast (e.g., Mazzoldi et al. 2012), as a composition of fault material and host rock may be similar, both being dominated by phyllosilicates. Analysis of microseismic activity following hydraulic stimulation in unconventional reservoirs has shown that induced inelastic damage is underestimated as clay-rich faults deform predominantly by aseismic slow slip (Zoback et al. 2012). Therefore, deformation of fault zones, induced damage and potential fluid migration pathways may remain undetected by seismicity measurements (Zoback and Gorelick 2012; Guglielmi et al. 2020, 2021). This increases uncertainties in hazard assessment during the site characterization process in this type of host rock. To better assess the evolution of mechanical and hydraulic properties during site operations, a detailed knowledge of the deformation behavior of phyllosilicate-dominated faults intersecting clay-rich rock formations and the underlying deformation mechanisms is required.

OPA has been studied extensively under in-situ conditions at the Underground Rock Laboratory (URL) Mont Terri (Thury and Bossart 1999; Bossart and Milnes 2017). There, the "Main Fault" crossing the URL provides an opportunity to study the structural, petrophysical and hydro-mechanical properties of representative tectonic structures. The heterogeneous architecture of the up to 5 m thick fault zone constitutes scaly clay (Vannucchi et al. 2003), slickensides on fractures, mineralized veins, anastomosing networks of µm-thin shear zones and fault gouge (Nussbaum et al. 2011; Laurich et al. 2014, 2017, 2018; Jaeggi et al. 2017), resulting in complex fault rupture behavior and modification of hydraulic properties when reactivated by gallery excavation and fluid injection (e.g., Guglielmi et al. 2017, 2020, 2021; Wenning et al. 2021; Hopp et al. 2022).

In several upper crustal fault zones located in different tectonic settings, the presence of clay minerals has been found to influence hydro-mechanical and frictional properties, fault weakness and strain accumulation by aseismic creep and slow slip (e.g., Faulkner et al. 2003; Fagereng and Sibson 2010; Schleicher et al. 2010; Collettini et al. 2019). Laboratory friction experiments have been performed on a variety of natural and synthetic fault gouges with varying proportions of different phyllosilicates showing that these minerals exhibit a low friction coefficient ($\mu = 0.03–0.5$) relative to other rock types (e.g., granite, sandstone), whose friction coefficients are generally in the range of $\mu = 0.6–0.85$ (Byerlee 1978). In addition, the frictional strength of the gouge decreases with increasing clay fraction (e.g., Logan and Rauenzahn 1987; Crawford et al. 2008; Tembe et al. 2010; Giorgetti et al. 2015; Ruggieri et al. 2021). In the framework of rate and state constitutive friction laws (e.g., Dieterich 1972; Ruina 1983; Marone 1998), the majority of clays revealed velocity-strengthening behavior at sliding velocities < 1 cm/s as well as limited frictional healing, suggesting that these minerals have a stabilizing effect on faults, inhibiting earthquake nucleation and rupture propagation (Bos and Spiers 2000; Niemeijer and Spiers 2006; Tesei et al. 2012; Giorgetti et al. 2015; Carpenter et al. 2016; Ruggieri et al. 2021). However, the frictional behavior of clays is complex and depends on several factors such as crystal structure, presence and chemistry of fluids, stress, temperature and strain rate (e.g., Saffer and Marone 2003; Moore and Lockner 2004; Ikari et al. 2007, 2009; Behnsen and Faulkner 2012; den Hartog et al. 2012a, b). Due to their low permeability, water-saturated clay-rich rocks may be further weakened at seismic slip rates by thermal pressurization and/or fluid pressurization induced by shear-enhanced compaction, causing high fluid pressures (e.g., Faulkner et al. 2011; Behnsen and Faulkner 2012; Bullock et al. 2015). Clay minerals also influence the fabric of crustal faults (e.g., Faulkner et al. 2003; Vannucchi et al. 2003; Collettini et al. 2009b; Fagereng and Sibson 2010; see Collettini et al. 2019 and reference therein) and promote the development of interconnected, anastomosing shear zones. Increasing fabric intensity further reduces frictional strength when compared to pulverized gouge produced from the same natural material, as was shown in laboratory tests (e.g., Collettini et al. 2009a; Niemeijer et al. 2010; Orellana et al. 2018a).

In accordance with previous laboratory friction experiments, wet gouge and scaly clay from OPA revealed low frictional strength ($\mu < 0.5$), a lack of re-strengthening and velocity-strengthening behavior (Orellana et al. 2018a, b, 2019), suggesting that faults in OPA could be easily reactivated and slip via aseismic creep. On the other hand, dry OPA gouge revealed velocity-weakening behavior and unstable sliding at shear velocities < 10 µm/s (Orellana et al. 2019). Even though natural fault zones are barely dry, desaturation of the host-rock is expected during the open drift stage of the repository and due to heat-generation as a result of radioactive decay of the emplaced nuclear waste (Tsang et al. 2012).

The mechanical behavior of intact OPA is strongly dependent on water saturation, with strength and stiffness increasing as the degree of saturation decreases, favoring brittle deformation (e.g., Nüesch 1991; Wild et al. 2015; Zhang and Laurich 2019; Schuster et al. 2021). Embrittlement reduces the sealing capacity of clay-rich cap-rocks and increases the leakage along potential faults (Ingram and Urai 1999) as well as the risk for seismicity during fault reactivation (Rutqvist et al. 2016). Brittle deformation of clay-rich rocks is favored with decreasing clay mineral content and is further influenced by the present stress field and burial history (e.g., Gutierrez et al. 1996; Ingram and Urai 1999; Nygård et al. 2006; Bourg 2015). At the Mont Terri URL, several sub-units have been distinguished within the formation, which vary in grainsize, color as well as the proportions of the main mineral components: phyllosilicates, quartz and carbonates (Hostettler et al. 2017; Lauper et al. 2018, 2021; Kneuker and Furche 2021). Accordingly, OPA is generally subdivided into a carbonate-rich sandy, a shaly and a sandy lithofacies type at the URL (Thury and Bossart 1999; Pearson et al. 2003). The compositional variability is also reflected in the rock properties of the different facies. Hence, the quartz-rich sandy facies displays a higher shear strength and stiffness compared to the clay-rich shaly facies (Popp and Salzer 2007; Siegesmund et al. 2014; Schuster et al. 2021).

As shown in the Mont Terri URL, discontinuities and mineralogical heterogeneity are to be expected in a future repository in OPA. Consequently, a detailed knowledge of the mechanical and frictional behavior of faults or fractures and their interaction with the different surrounding lithofacies types is required to predict construction-related damage and long-term integrity. To date, few experimental studies have focused on host-rock heterogeneity and characterized the mechanical properties of the sandy facies of OPA (Zhang and Laurich 2019; Crisci et al. 2021; Schuster et al. 2021). In addition, most deformation experiments on OPA are limited to intact rock samples (e.g., Nüesch 1991; Amann et al. 2012; Wild and Amann 2018; Zhang and Laurich 2019; Schuster et al. 2021), resulting in a lack of laboratory studies characterizing the mechanical properties of faulted OPA taking compositional heterogeneities into account.

Here we performed a series of triaxial tests to investigate the impact of mineral composition and confining pressure on fault reactivation and deformation behavior of dry OPA, using cylindrical saw-cut samples from the shaly and sandy facies. Macroscopic observations, elastic P-wave velocity and AE measurements, and microscopic analysis using electron microscopy were combined to describe the deformation behavior, fault stability, gouge production, strain partitioning between localized fault slip and distributed off-fault matrix deformation as well as to study the prevailing microdeformation mechanisms. After a fixed shear displacement, slide-hold-slide tests were additionally performed to study fault healing and restrengthening.

2 Materials and Methods

2.1 Sample Characterization and Preparation

Samples from the shaly and sandy facies were obtained from the OPA formation collected at a depth of approximately 300 m in the Mont Terri URL (Thury and Bossart 1999; Hostettler et al. 2017). The Jurassic-aged OPA (Toarcian to Aalenian) was deposited in a shallow-marine environment and experienced a maximum burial depth of 1.35 km and a maximum temperature of 85 °C (Mazurek et al. 2006). Therefore, OPA exposed at the Mont Terri URL is over-consolidated. Core material of OPA was provided by Swisstopo (Federal Office for Topography, Wabern, Switzerland) and originates from borehole BMA-4 (shaly facies) and BCL-2 (sandy facies) at the Mont Terri URL. Drill cores of 101 mm diameter were recovered under dry conditions using compressed air as a cooling agent. After extraction, the cores were stored in plastic liners and vacuum-sealed in aluminum foil preventing desaturation.

The shaly facies (Fig. 1b, d) is composed of rather homogeneous, dark-grey, laminated, argillaceous claystones mainly consisting of clay minerals (illite, illite–smectite kaolinite and chlorite) with silt to fine-sand sized bioclasts (e.g., fossil shells) and detrital quartz and feldspar grains dispersed throughout the clay-rich matrix (Kneuker and Furche 2021; Lauper et al. 2021). The OPA sandy facies (Fig. 1a, c) is a heterogeneous, siliceous-argillaceous claystone, characterized by an alternation of dark-grey, clay-rich layers and undulating lenses and layers of silt to sand-sized quartz and feldspar grains, cemented by carbonates (Lauper et al. 2018, 2021; Schuster et al. 2021). Well-pronounced bedding planes of OPA are caused by the preferential alignment of phyllosilicates, leading to a transverse isotropy of petrophysical, mechanical and hydraulic properties (e.g., NAGRA 2002; Wenk et al. 2008; Siegesmund et al. 2014; Favero et al. 2018; Schuster et al. 2021).

For each facies type, cylindrical samples with a final diameter of 50 mm were drilled perpendicular to the bedding. Cylindrical specimens were precision ground to 102 mm length and cut in half at an angle of $\theta = 30°$ oriented to the cylinder axis. Cutting and polishing of fault surfaces resulted in a final sample length of $L = 101 \pm 1$ mm. Roughness of the saw-cut fault planes was produced by hand polishing using #180 grit silicon carbide abrasive grinding paper. To ensure a comparable initial roughness of the samples, roughened surfaces were scanned using a 3D optical profilometer. Average RMS (root mean square) roughness was $S_q = 7.9 \pm 2.0$ µm (cf., chapter 2.3). All preparation steps

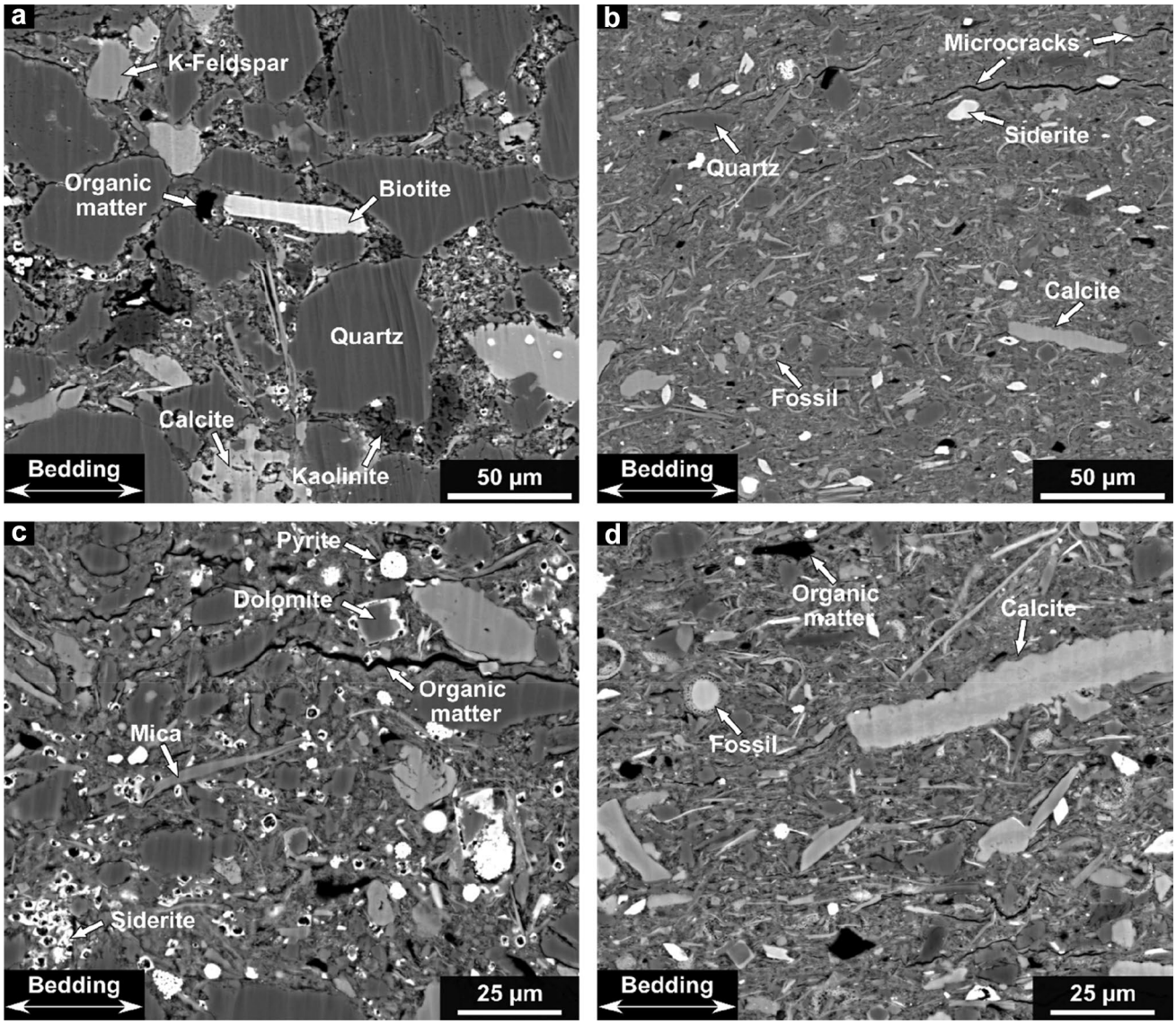

Fig. 1 Backscattered electron microscope images of undeformed Opalinus Clay of the sandy (**a**, **c**) and shaly facies (**b, d**), showing microstructural differences in both facies' types as well as predominant mineral phases. **a** Sand layer of the sandy facies, characterized by a grain-supported framework of clastic mineral phases with barely compacted clay matrix filling the interparticle space. **b** The shaly facies is more homogeneous compared to the sandy facies with smaller grain sizes of clastic minerals. **c** Mineral grains in clay layers of the sandy facies display a smaller grain size compared to sand layers and are surrounded by clay matrix. Microstructures of clay layers of the sandy (**c**) and the shaly facies (**d**) appear similar. However, clay layers of the sandy facies display a higher content of quartz, whereas calcite is more abundant in the shaly facies

were performed under dry conditions, keeping exposure to the laboratory environment to a minimum.

After preparation, the specimens and several sub-samples, prepared from the remaining core material, were dried in an oven at a temperature of 50 °C with a relative humidity of $22 \pm 5\%$ until a constant weight was reached. Residual water content was determined by drying sub-samples at 110 °C for > 48 h. It is on average ~ 1.0 wt% for shaly and ~ 0.4 wt% for the sandy facies' samples, respectively. Sub-samples were used to estimate the connected porosity (φ) of samples from both facies' types, determined from skeletal and bulk density. Grain density was measured using a He-pycnometer (Micrometrics, AccuPyc 1340) and bulk density (ρ) was determined from the ratio of sample weight and volume. Bulk density is 2.30 ± 0.02 g/cm^3 for the shaly facies and 2.37 ± 0.01 g/cm^3 for the sandy facies with connected porosities φ of 15.7 ± 1.3 and 11.1 ± 1.1 vol%, respectively. At the microscale, we observe several bedding-plane-parallel intergranular microcracks (Fig. 1b) in the undeformed samples, especially in shaly facies' samples,

Table 1 Bulk mineralogy of the sandy and shaly facies of Opalinus Clay obtained from sub-samples of used core sections

Opalinus Clay	Clay (wt%)	Quartz (wt%)	Carbonates (wt%)	Feldspar (wt%)	Pyrite (wt%)
Sandy facies	36	42	10	11	< 1
Shaly facies	74	9	11	5	< 1

that potentially originate from stress relaxation during core drilling (e.g., Corkum and Martin 2007) and/or drying (e.g., Soe et al. 2009). These microcracks can account for up to 28 vol.% of porosity (Houben et al. 2013, 2014) and may be effectively closed under laboratory conditions at confining pressures ≥ 6 MPa (e.g., Winhausen et al. 2020).

Bulk mineralogy was determined using a PANalytical Empyrean X-ray diffractometer (XRD), operating at 40 kV and 40 mA with Cu-Kα radiation and a step size of 0.013°2θ from 4.6° to 85°. Major mineralogical phases were determined with the program EVA by Bruker (version 11.0.0.3) and quantified (± 3 wt%) by Rietveld refinement using BGMN software and Profex (version 3.10.2, Doebelin and Kleeberg 2015). Determined bulk mineralogical composition of both facies is listed in Table 1. Consistent with previous studies (e.g., Thury and Bossart 1999; Pearson et al. 2003; Bossart and Milnes 2017), the sandy facies reveals a higher content of quartz (42 wt%) and feldspars (11 wt%) with a lower proportion of clay minerals (36wt%) compared to the shaly facies of OPA.

A pair of biaxial stacked rosette strain gauges was glued on the sample surface at the center of the upper and lower block of each specimen, which allowed the recording of the bulk vertical and radial matrix strain during axial deformation. Four additional single strain gauges were attached to the lower sample block at a distance of 3 mm to the saw-cut plane to monitor local strains parallel and perpendicular to the saw-cut fault plane (see Fig. S1a, b of the supporting material). To prevent intrusion of oil (confining medium), the saw-cut sample blocks were inserted into a neoprene jacket of 2 mm thickness. Acoustic emissions (AE) and ultrasonic velocities were measured with 14 piezoelectric P-wave transducers (1 MHz resonant frequency) encapsulated into brass housings of 1 cm diameter that were glued on the sample surface at perforations of the neoprene jacket using epoxy (see Fig. S1a). An additional pair of P-wave transducers was installed in the top and bottom steel plugs of the triaxial cell. This sensor setup ensured the recording of elastic P-wave velocities along different ray paths through the sample and AE localization.

2.2 Experimental Setup and Procedure

Triaxial deformation tests were performed at room temperature using a servo-hydraulic loading frame (Material Testing Systems, MTS; Stanchits et al. 2011). Prior to applying axial load, all tested saw-cut samples were hydrostatically precompacted at 50 MPa pressure for 18 h to ensure comparable initial asperity damage and matrix compaction for each sample. Subsequently, each saw-cut sample was unloaded to the respective target confining pressure (p_c = 5, 20 or 35 MPa) at a similar rate (1 MPa/min) as during loading. With the chosen confining pressure range, we intended to simulate the target depths of future repository sites (< 1000 m depth). Triaxial tests were conducted at a constant axial piston displacement rate of 1 µm/s. The total axial shortening of the specimen (D_{tot}) was determined from the piston displacement (D_{LVDT}) measured externally by a linear-variable displacement transducer (LVDT). Experiments were terminated after $D_{LVDT} \approx 6.75$ mm to prevent slip-induced jacket rupture and reduce geometry effects leading to stress and or strain inhomogeneities. Piston displacement readings were corrected for both system compliance and stiffness of the loading frame (≈0.67–0.7 MN/mm) resulting in a true sample axial deformation rate of ~ 0.88 µm/s. Total axial strain ($\varepsilon_{tot} = D_{tot}/L \times 100\%$) was determined from the initial sample length (L) and corrected axial shortening of the specimen (D_{tot}). Axial strain was partitioned into matrix strain of the saw-cut blocks ε_{ax} measured with strain gauges and slip (s_f) along the saw-cut given by $s_f = (D_{tot} - \varepsilon_{ax} \times L)/cos\ \theta$ (see Fig. S1b). Strain partitioning (%) is expressed by the ratio of matrix strain ε_{ax} to a total axial strain of the sample ε_{tot}. Volumetric matrix strain was calculated by $\varepsilon_{vol} = \varepsilon_{ax} + 2 \times \varepsilon_{rad}$ from averaged axial and radial stain gauge readings of the saw-cut blocks. Axial stress (σ_1) was measured with a resolution of about ± 0.5 MPa by an external load cell corrected for sealing friction of the loading piston. Stiffness and friction were determined in calibration runs at relevant confining pressures using stainless steel cylinders. Shear (τ) and normal stress (σ_n) acting on the fault plane were derived from principal stresses using $\tau = ½ \times (\sigma_1 - p_c) \times sin\ 2\theta$ and $\sigma_n = ½ \times [(\sigma_1 + p_c) - (\sigma_1 - p_c) \times cos\ 2\theta]$. Shear and normal stresses were corrected for the progressively reducing contact area along the inclined saw-cut during deformation (Tembe et al. 2010). Amonton's friction coefficient (μ) resolved on the saw-cut plane was determined by the ratio of shear to normal stress assuming no cohesion. Mechanical data were sampled at a rate of 10 Hz during axial deformation.

In an effort to evaluate creep relaxation and static frictional strengthening characteristics of artificially fractured OPA, we performed slide-hold-slide (SHS) tests (e.g., Dieterich 1972; Beeler et al. 1994; Marone 1998; Carpenter et al. 2016) for each sample. Axial displacement was first stopped

after a piston displacement of $D_{LVDT} \approx 6$ mm for a holding period of $t_h = 60$ s. Subsequently, samples were re-sheared for $D_{LVDT} = 0.25$ mm at an axial displacement rate of 1 µm/s, followed by a second and third holding period of 600 and 6000 s, respectively. For the sample of the sandy facies that was deformed at $p_c = 5$ MPa, the piston was stopped at $D_{LVDT} \approx 7$ mm. Furthermore, for technical reasons, the experiment was interrupted during the third holding period, which is why only the first two periods were conducted. Following Karner et al. (1997) and Marone (1998), we determined from SHS tests (1) the reduction of friction ($\Delta\mu_c$) due to stress relaxation (difference between pre-hold friction coefficient and the value attained at the end of the hold period), (2) frictional strengthening ($\Delta\mu_h$) after reloading (difference between peak friction upon re-shear and the friction value prior to hold, corrected for strain hardening trends by linear trend lines connecting slide phases) and (3) frictional weakening $\Delta\mu_w$ and the respective weakening distance d_w (see Fig. S2a, b of the supporting material).

Full waveform AE signals as well as ultrasonic velocity signals were recorded at a sampling rate of 10 MHz and an amplitude resolution of 16 bits with a 16-channel transient recording system (DAXBox, Prökel). P-wave velocity measurements were performed using seven sensor pairs located on opposite sides of the sample surface and one pair on the top/bottom of the sample (see Fig. S1). Active ultrasonic transmission (UT) measurements were performed every 15 s throughout the whole experiment. P-wave travel times were picked using the Akaike information criterion (AIC) criterion and corrected for sample deformation and fault slip. UT measurements provided time-dependent quasi-anisotropic P-wave velocity model composed of five horizontal and one vertical layer that was further used to locate AE events (e.g., Stanchits et al. 2011; Goebel et al. 2014; Kwiatek et al. 2014). For AE localization, signals were first amplified by 40 dB and high-pass filtered at 100 kHz (Physical Acoustic Corporation). P-wave arrival times were automatically picked using AIC and convolutional neural network (e.g., Ross et al. 2018). To locate AE events, we used the Equivalent Differential Time method (e.g., Font et al. 2004), with the inverse problem solved using a combination of grid search followed by a simplex search technique. The average AE hypocenter location accuracy is ± 2 mm (Stanchits et al. 2011).

2.3 Microstructural Imaging

Top and bottom saw-cut fault surface topography of each sample was measured before and after deformation using a high resolution (0.1 µm) white light optical profilometer (Keyence VR3200) with a *Z*-axis measurement accuracy of ± 3 µm. Microtopography areas of 50 × 40 mm^2 (1062 × 850 px) were acquired at the same starting points to evaluate surface evolution.

Using a scanning electron microscope (FEI Quanta 3D Dual Beam), microstructural imaging was performed on samples that were selected from deformed specimens prepared parallel to shear displacement. The fault area of interest was first covered with epoxy resin to maintain microstructures (gouge and off-fault microstructures). Rectangular-shaped specimens (11 × 8 × 3 mm^3) were then cut and pre-polished by hand with SiC grinding paper down to P4000 grit for subsequent broad ion beam (BIB) polishing (JEOL IB-19520CCP). BIB polishing for 2 h at 8 kV, 200 µA and 6 h at 6 kV, 150 µA, removed a layer of approximately 100 µm thickness on an area of ~ 2.5 mm^2. Additional samples of the (unpolished) fault surface were prepared to examine topography microstructures. Scanning electron microscopy (SEM) was performed on carbon-coated samples at an acceleration voltage of 20 kV and a working distance of 5 mm. Mineral phases were determined with an attached EDAX energy-dispersive X-ray analyzer (EDX).

3 Results

In total, we conducted six triaxial deformation tests on saw-cut samples of OPA. Samples from the sandy and shaly facies were deformed at confining pressures of $p_c = 5$, 20 and 35 MPa with axial deformation rates of ~ 0.88 µm/s. Tests were performed at room temperature on cylindrical samples drilled perpendicular to bedding orientation and containing a saw-cut fault plane inclined at 30° to the loading direction. This set of experiments allows us to investigate the influence of sample composition and confining pressure on the localization behavior during reactivation of the fault plane, including AE activity as well as P-wave velocity evolution during deformation, and creep relaxation during hold periods.

3.1 Mechanical Data

3.1.1 Fault Reactivation and Frictional Behavior

The stress–strain behavior of samples from both facies types is strongly affected by the applied confining pressure. The differential stress ($\sigma_d = \sigma_1 - p_c$) of the assembly significantly increases with pressure and exhibits pronounced strain hardening at $p_c = 20$ and 35 MPa (Fig. 2a, b, Table 2). The initial phase of elastic loading up to the yield stress σ_y (marked with stars in Fig. 2a, b) persists up to a total axial strain between $\varepsilon_{tot} = 0.14$–1.2%. The yield stress indicates the onset of plastic deformation of sample blocks.

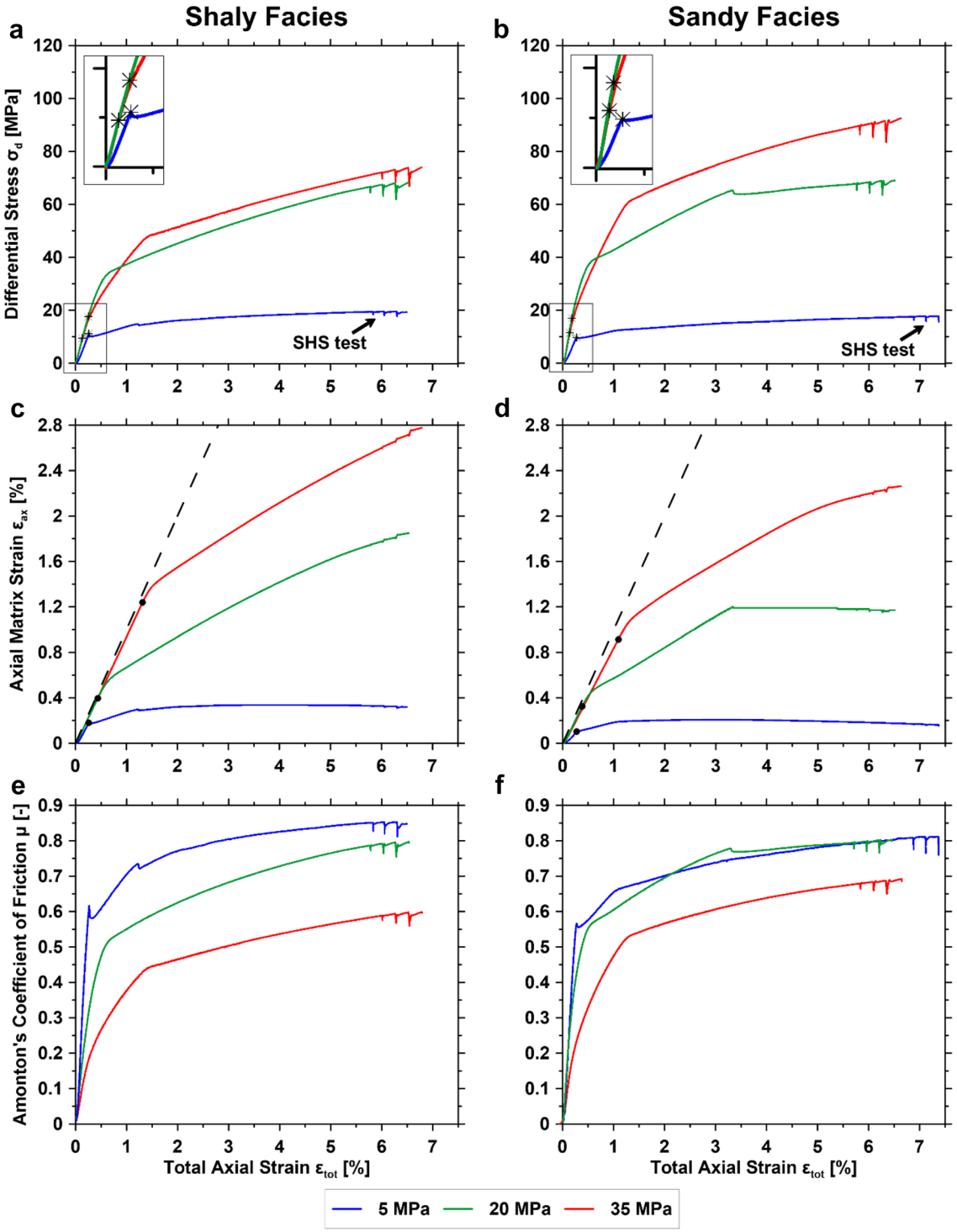

Fig. 2 Mechanical data of fault reactivation experiments performed on the shaly (left column) and sandy facies (right column) of Opalinus Clay. Differential stress-total axial strain curves (**a**, **b**) showing the influence of confining pressure on deformation behavior. Yield stress σ_y is indicated by stars (enlarged section). Vertical matrix strain measured by strain gauges is plotted against total strain (**c**, **d**), indicating the degree of strain partitioning between fault slip and matrix compaction. Black dashed line represents a slope of 1, which corresponds to a fully locked fault. Black dots represent stress σ_f at the onset of slip-along saw-cut faults. Plots of Amonton's friction coefficient μ versus total axial strain (**e**, **f**) highlights the influence of facies type and confining pressure on strain hardening

Table 2 Summary of experimental parameters and mechanical data

Opalinus Clay	p_c (MPa)	σ_y (MPa)	σ_f (MPa)	Stress at $\varepsilon_{tot}=5\%$ (MPa)	Total D_{tot} (mm)	Total s_f (mm)	Strain partitioning (%)	Slip events*	Stress drop (MPa)	d_w (µm)	v_{sf} (µm/s)
Sandy facies	5	9.4	9.8	16.5	7.444	8.418	3	1. $\varepsilon_{tot}=0.28$	0.3	4.9	1.2
Sandy facies	20	17.0	32.2	66.7	6.599	6.256	18	1. $\varepsilon_{tot}=3.33$	1.5	5.7	2.2
Sandy facies	35	11.5	55.4	88.3	6.628	5.034	34	–	–	–	–
Shaly facies	5	11.1	11.1	19.0	6.673	7.244	5	1. $\varepsilon_{tot}=0.27$	1.0	6.9	2.2
								2. $\varepsilon_{tot}=1.23$	0.5	5.8	2.1
Shaly facies	20	17.6	27.8	63.3	6.783	5.451	28	–	–	–	–
Shaly facies	35	9.4	46.5	67.7	6.548	4.468	41	–	–	–	–

p_c confining pressure, σ_y yield stress bulk matrix, σ_f stress at onset of fault slip, ε_{tot} total axial strain, D_{tot} LVDT displacement, s_f fault slip, *number of slip events at total axial strain ε_{tot} (%), d_w slip weakening distance, v_{sf} slip rate

At 5 MPa confining pressure, axial matrix strain ε_{ax}, inferred from axial strain gauges glued to the saw-cut blocks, increases initially at a similar rate as total axial strain ε_{tot} (Fig. 2c, d), i.e. the fault is locked. At stress σ_f fault slip initiates, and axial shortening is progressively accommodated by fault slip (marked with dots in Fig. 2c, d). For the samples deformed at $p_c = 5$ MPa, σ_f closely corresponds to yield stress σ_y (Fig. 2). We observe a small stress drop of ~ 0.3 and ~ 1 MPa for sandy facies and shaly facies samples, respectively (Fig. 2a, b, Table 2). Subsequently, the shaly facies sample shows minor strain hardening until a second stress drop of ~ 0.5 MPa occurs at $\varepsilon_{tot} \sim 1\%$, followed by a progressive decrease in hardening to an almost steady state stress level. The sandy facies sample also hardens up to $\varepsilon_{tot} \sim 1.1\%$, but without a stress drop. Subsequently, strain hardening is decreasing with increasing strain. Beyond $\varepsilon_{tot} \sim 1.1$–$1.2\%$ matrix strain stops increasing and sample shortening is predominantly accommodated by fault slip (Fig. 2c, d). Friction coefficients at fault reactivation μ are ~ 0.62 for shaly and 0.57 for sandy facies samples, respectively (Fig. 2e, f).

Samples that were deformed at confining pressures of 20 and 35 MPa display yielding (stars in Fig. 2a, b) followed by continuous strain hardening. Yield stress σ_y and stress level at onset of slip σ_f progressively deviate with increasing confining pressure with $\sigma_f > \sigma_y$. After fault slip starts at stress σ_f, vertical matrix strain increases at a progressively declining rate. Consequently, strain partitioning into matrix deformation of saw-cut blocks and fault slip evolves nonlinearly. No stress drops were observed except for the sandy facies sample deformed at $p_c = 20$ MPa. For this sample, the axial matrix strain stays constant after a stress drop of ~ 1.5 MPa at $\varepsilon_{tot} \sim 3.3\%$, and sample shortening occurred by localized fault sliding only.

Up to stress σ_f at which sliding starts (dots in Fig. 2c, d), the fault remains almost completely locked and matrix strain increases at almost the same rate as the total axial strain. During this initial deformation ~ 95% shortening is accommodated by the deformation of the sample blocks. With increasing confining pressure, the accumulated axial matrix strain and the stress at fault reactivation increase for samples from both facies. Partitioning of total sample strain into axial matrix strain increases (Fig. 2c, d). The ratio of shear stress to normal stress (friction coefficient μ) decreases with increasing confining pressure, in particular for shaly facies samples (Fig. 2e, f). The friction coefficients at fault reactivation of the sandy facies at $p_c = 20$ and 35 MPa are $\mu \sim 0.53$ and 0.49 respectively, slightly higher compared to the shaly facies at similar pressures ($\mu \sim 0.45$ and 0.43, respectively).

At 5 and 20 MPa confining pressure, we observed a few stick-slip events with small stress drops. Slip rates of events did not significantly exceed stable slip rates and ranged between 1.1 and 1.5 µm/s, corresponding to slip rates along

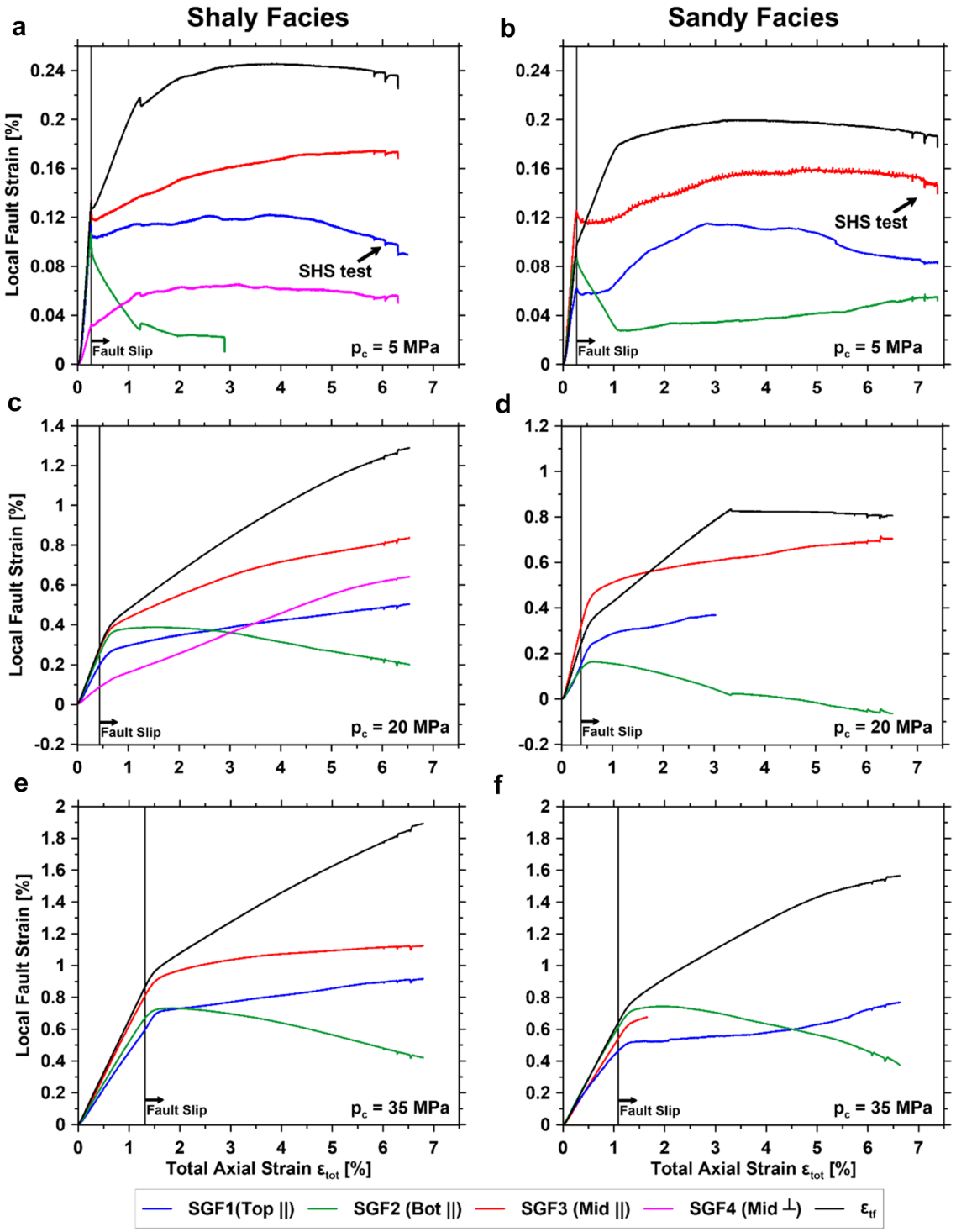

Fig. 3 Local strain measured parallel (SGF1-SGF3) and perpendicular (SGF4) to the saw-cut fault plane as a function of total axial shortening ε_{tot} for the shaly (left column) and sandy (right column) facies of Opalinus Clay deformed at 5 (**a**, **b**), 20 (**c**, **d**) and 35 (**e**, **f**) MPa confining pressure. Strain gauges are attached along the lower sample block at a distance of 3 mm to the fault plane (see Fig. S1a of the supporting material). ε_{tf} shows the fault parallel strain transformed from axial and radial strain measured on the sample blocks. Note that some strain gauges are not shown or are only partially shown because they failed during the experiment. Vertical lines indicate the onset of fault slip determined from axial strain gauges (cf. dots in Fig. 2c, d)

the fault of $v_{sf} = 1.3–1.7$ µm/s. Stable slip rates along the fault range between 1.0 and 0.8 µm/s for the shaly facies and between 1.2 and 0.9 µm/s for the sandy facies saw-cuts, once slip is dominantly accommodating deformation, but depending on strain partitioning. In all samples, fault slip rates decrease with increasing confining pressure. We used four single strain gauges attached to the lower sample block in order to measure localized deformation parallel (SGF1–3) and perpendicular (SGF4) to the fault at a distance of 3 mm (Fig. 3, see Fig. S1a). As observed for the axial strain gauges (Fig. 2a, c), strain along the fault increases linearly with total axial strain ε_{tot} at the beginning, independent of the applied confining pressure and in all facies, indicating a locked fault. At 5 MPa confining pressure, we observe an abrupt release of strain measured on all fault strain gauges for both facies at reactivation. On the other hand, at elevated pressure no dynamic strain release is observed as the fault starts sliding (Fig. 3c–f). Instead, measured fault strain starts to develop nonlinearly with increasing total axial strain when stress σ_f is reached. Generally, the onset of fault slip determined from axial strain readings (dots in Fig. 2c, d) agrees with the beginning of this non-linear increase in fault strain (Fig. 3 vertical lines).

Assuming homogeneous deformation of the sample blocks, we transformed the measured axial ε_{ax} and radial ε_{rad} strain to predict fault parallel strain using the expression $\varepsilon_{tf} = \varepsilon_{ax} \times cos\ 2\theta + \varepsilon_{rad} \times cos\ 2\theta$ (Jaeger et al. 2007). Before sliding is initiated, we find the transformed strain in good agreement with the strain measured by the parallel-oriented strain gauges, suggesting homogeneous strain distribution within the sample. After reactivation, we observe a uniform behavior of the strain gauges oriented parallel to the fault in all samples. With continuing total axial shortening after reactivation, fault parallel strain measured at the top and in the middle of the sample increases with a decreasing rate, while the strain gauges attached at the bottom of the fault show a release of strain. Furthermore, parallel strain transformed from axial and radial strain readings increasingly deviates after reactivation and with increasing confining pressure. The measurements suggest a heterogeneous strain and probably stress distribution along the saw-cut fault plane with non-uniform amounts of local slip being accommodate once slip is initiated. In addition, the deviation from transformed and measured parallel strain suggests higher strain relaxation close to the fault than in the sample blocks.

3.1.2 Slide-Hold-Slide Test

With the exception of the sandy facies sample deformed at 5 MPa confining pressure ($D_{LVDT} \sim 7$ mm), we performed slide-hold-slide (SHS) tests on each specimen after a total piston displacement of $D_{LVDT} \sim 6$ mm. Due to the applied confining pressure and different strain hardening behavior of the samples, differential stress reached at the start of SHS test (σ^H_d) varies. Hold times were 60, 600 and 6000 s and axial displacement after each hold period was 0.25 mm. During each period, the differential stress relaxed nonlinearly as elastic strain stored in the specimen and loading frame was released, resulting in sample creep (Fig. 4). Note, that in our experimental setup both the normal and shear stresses acting on the fault plane decreased during each hold period.

For samples from both facies types deformed at varying confining pressures, differential stresses decrease with increasing hold time, with increasing confining pressure and with larger initial σ^H_d (Fig. 4). After each hold period, elastic loading is terminated by a small stress drop once sliding on the saw-cut fault is activated (Table 3). Peak stresses achieved during loading increase with hold time, confining pressure and σ^H_d. However, at confining pressure of 35 MPa (Fig. 4e, f) initial peaks and stress drops become less prominent for the shaly facies sample.

Stress relaxation was similar for all hold periods lasting different time intervals. Here, we focus on the effect of confining pressure on the hold period of 6000 s (Fig. 5) and measure axial and volumetric matrix strain and differential stress during the hold periods. Positive strain represents compaction and negative strain indicates dilatancy. The shaly facies sample deformed at 5 MPa confining pressure and the sandy facies samples deformed at 5 and 20 MPa confining pressure started dilating prior to SHS tests (Fig. 2). During stress relaxation, these specimens continue to dilate (Fig. 5a–d). This is in contrast to shaly facies samples deformed at 20 and 35 MPa confining pressure. During relaxation, axial and volumetric strain change from dilation to compaction within < 1000 s. Similar behavior is observed for the sandy facies sample deformed at 35 MPa confining pressure.

For sandy and shaly facies samples, we observed increasing creep relaxation $\Delta\mu_c$ with increasing hold time but smaller $\Delta\mu_c$ at higher confining pressures (Figs. 4, 6a, b). Samples from sandy and shaly facies behaved similar at comparable conditions unlike sample response to reloading that depended on OPA facies type. For the shaly facies of Opalinus Clay, strengthening $\Delta\mu_h$ is negative independent of hold time and confining pressure (Fig. 6c) and the total amount of frictional strengthening decreases with increasing confining pressure but increases with increasing hold time. For the sandy facies frictional strengthening is negative at $p_c = 5$ MPa but close to zero at higher confinement at hold times of 60 and 600 s (Fig. 6d). At 6000 s, strengthening at $p_c = 20$ and 35 MPa is again slightly negative.

With the exception of the two experiments on sandy facies samples, creep relaxation and frictional strengthening follow a linear dependence with increasing hold time on semilogarithmic scale (Fig. 6). Following previous studies

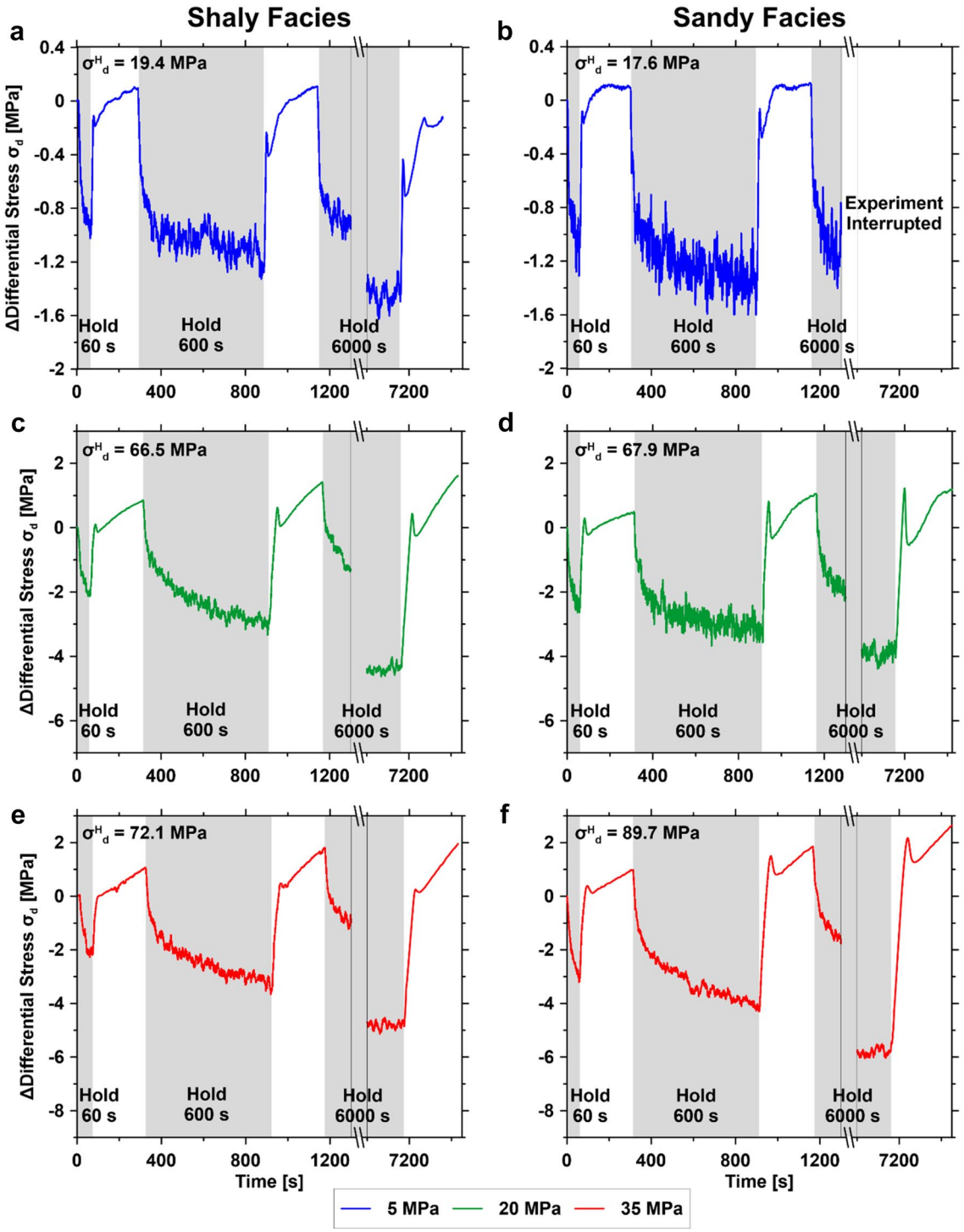

Fig. 4 Slide-hold-slide tests performed on the shaly and sandy facies of Opalinus Clay deformed at confining pressures of $p_c = 5$, 20 and 35 MPa. During each hold period, ranging from 60 to 6000 s (indicated by grey areas and numbers), differential stress decreases as elastic strain stored in the sample and loading frame is relaxed. Note that differential stress $\Delta\sigma_d$ and time are all normalized to the start conditions of the first hold (60 s). Furthermore, note the broken time axis and different scales for $\Delta\sigma_d$ axis. Different initial differential stresses at the start of SHS tests (σ^H_d) are due to confining pressure and strain-hardening behavior

Table 3 Summary of mechanical data from the observed stress drops that followed each hold period

Opalinus Clay	p_c (MPa)	Hold time sequence (s)	Stress drop (MPa)	d_w (µm)	v_{sf} (µm/s)
Sandy facies	5	60	0.1	10.6	1.2
		600	0.2	15.3	1.5
		–	–	–	–
Sandy facies	20	60	0.4	20.4	1.5
		600	1.0	31.9	2.3
		6000	1.6	37.0	3.7
Sandy facies	35	60	0.3	28.0	1.0
		600	0.7	31.9	1.5
		6000	0.9	41.2	1.6
Shaly facies	5	60	0.1	10.1	1.2
		600	0.2	13.1	1.5
		6000	0.3	18.6	1.5
Shaly facies	20	60	0.2	16.2	1.3
		600	0.6	24.3	1.7
		6000	0.7	30.9	1.8
Shaly facies	35	60	0.0	3.7	0.9
		600	0.1	16.2	1.1
		6000	0.1	20.3	1.1

p_c confining pressure, d_w slip weakening distance, v_{sf} slip rate

where SHS tests were performed on bare rock surfaces or natural and synthetic fault gouges of different compositions (e.g., Dieterich 1972; Marone 1998; Carpenter et al. 2016), creep relaxation rates (β_c) and frictional strengthening rates (β_h) may be expressed as $\beta_{c,h} = d(\Delta\mu_{c,h})/d(\log_{10}(t_h))$. Both rates obtained are negative for the conducted experiments (Fig. 6e, f). Measured creep relaxation rates of the shaly facies are lower compared to those of the sandy facies at $p_c \geq 20$ MPa and tend to decrease with increasing confining pressure, whereas β_c of the sandy facies is less affected by confining pressure (Fig. 6e). In contrast, frictional strengthening rates of both facies seem to increase slightly with increasing confining pressure (Fig. 6f), where β_h values of the sandy facies are higher compared to the shaly facies.

We observe a distinct peak in frictional strength upon reloading followed by a stress drop as fault slip starts. In general, the amount of frictional weakening $\Delta\mu_w$ and slip d_w are correlated as absolute values of both increase with increasing hold time (Fig. 7a, b). For all samples, weakening $\Delta\mu_w$ is less with increasing confining pressure and σ^H_d. For the sandy facies of OPA, slip weakening distance increases with increasing confining pressure, as for shaly facies samples deformed at $p_c = 5$ and 20 MPa. Furthermore, sandy facies samples displayed stronger frictional weakening $\Delta\mu_w$ and slip d_w at $p_c = 20$ and 35 MPa compared to the shaly facies.

To estimate the stability of the observed fault slips (during constant strain rate deformation and SHS tests), we have determined the unloading fault stiffness of OPA ($k_f = -\Delta\tau/\Delta s_f$) during each slip event, resulting in values between 4 and 34 MPa/mm. Instability may be promoted if the fault stiffness becomes greater than the system stiffness, i.e., a stiffness ratio $\kappa = k_s/k_f < 1$ (Rice 1983). To compare the given fault and system stiffness values, we projected k_f along the loading direction to obtain the equivalent axial stiffness of the fault, yielding values from 10 to 90 MPa/mm. For k_s, both the given machine stiffness ($k_m \approx 0.67$–0.7 MN/mm, corresponding to ~ 341–356 MPa/mm) and elastic rock matrix stiffness (k_r) have to be considered. Therefore, we determined Young's modulus E of each sample between the onset of deformation and yield stress. For the sandy and shaly facies, we obtain $E = 11$–14 GPa and 6–8 GPa, respectively, comparable to previous deformation experiments performed on OPA (e.g., Nüesch 1991; Schuster et al. 2021). Stiffness of the loading system is calculated via $k_s = 1/(1/k_r + 1/k_m)$, where rock matrix stiffness is estimated using the expression $k_r = E/L$. Depending on the facies type and confining pressure, loading system stiffness ranges between $k_s = 52$–100 MPa/mm. At none of the applied confining pressures the condition $\kappa = k_s/k_f < 1$ was met. We can therefore conclude that fault slip is stable and accommodated by slow slip.

3.2 Ultrasonic Velocities and AE Activity

We monitored elastic P-wave velocity evolution and AE activity during fault reactivation and present here three different velocity traces (see Fig. S1a, Fig. 8). P-wave velocity was measured parallel to the sample axis crossing the saw-cut plane, providing the velocity normal to bedding orientation $V_p(90°)$ (see Fig. S1a, sensor pairs: Z16-L15). P-wave velocity parallel to bedding orientation $V_p(0°)$ and perpendicular to the cylinder axis was measured at the top (V^T_p) and bottom (V^B_p) part of the sample at an offset of ~ 1.5 cm from the fault plane (see Fig. S1a, sensor pairs: I5-W7 and C11-R13).

P-wave velocity parallel to the bedding is higher than perpendicular to it (Fig. 8). Using the ratio of measured initial velocities parallel and perpendicular to foliation as a measure of anisotropy ($V_p(0°)/V_p(90°)$), the anisotropy of shaly facies samples (~ 1.7–1.9) exceeds that of sandy facies samples (~ 1.3–1.6). The differences between $V_p(0°)$ and $V_p(90°)$ decrease at elevated confining pressures and axial shortening. In comparison to previous axial deformation, sample relaxation and fault reactivation during SHS tests have no significant effect on P-wave velocities.

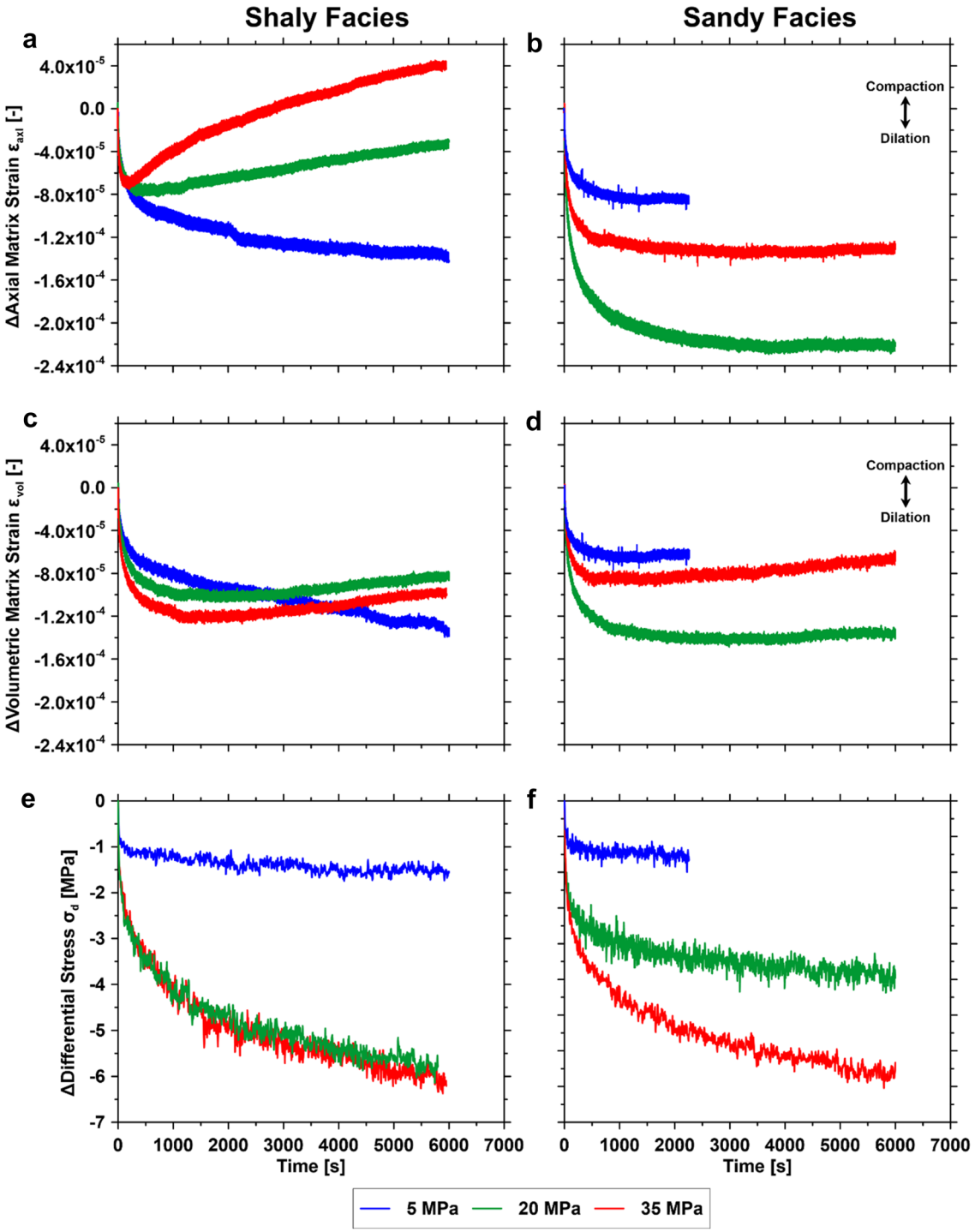

Fig. 5 Normalized axial ε_{ax} (**a**, **b**) and volumetric ε_{vol} (**c**, **d**) strain and differential stress σ_d as a function of time during stress relaxation with a hold period of 6000 s of the shaly (left column) and sandy facies (right column) of Opalinus Clay. Note that the test of the sandy facies sample deformed at a confining pressure of 5 MPa was interrupted after ~ 2000s due to technical issues

At 5 MPa confining pressure, bulk horizontal velocity $V^{B,T}_{p}$ (0°) of all samples ranges between 3.6 and 3.7 km/s and displays no significant change during axial deformation (Fig. 8a, b). In contrast, P-wave velocities measured parallel to the sample axis and normal to bedding V_p (90°) increase with increasing axial load. Initial velocity increase is about 180 m/s for the shaly and ~ 75 m/s for the sandy facies' samples, respectively, up to fault reactivation and stress drop.

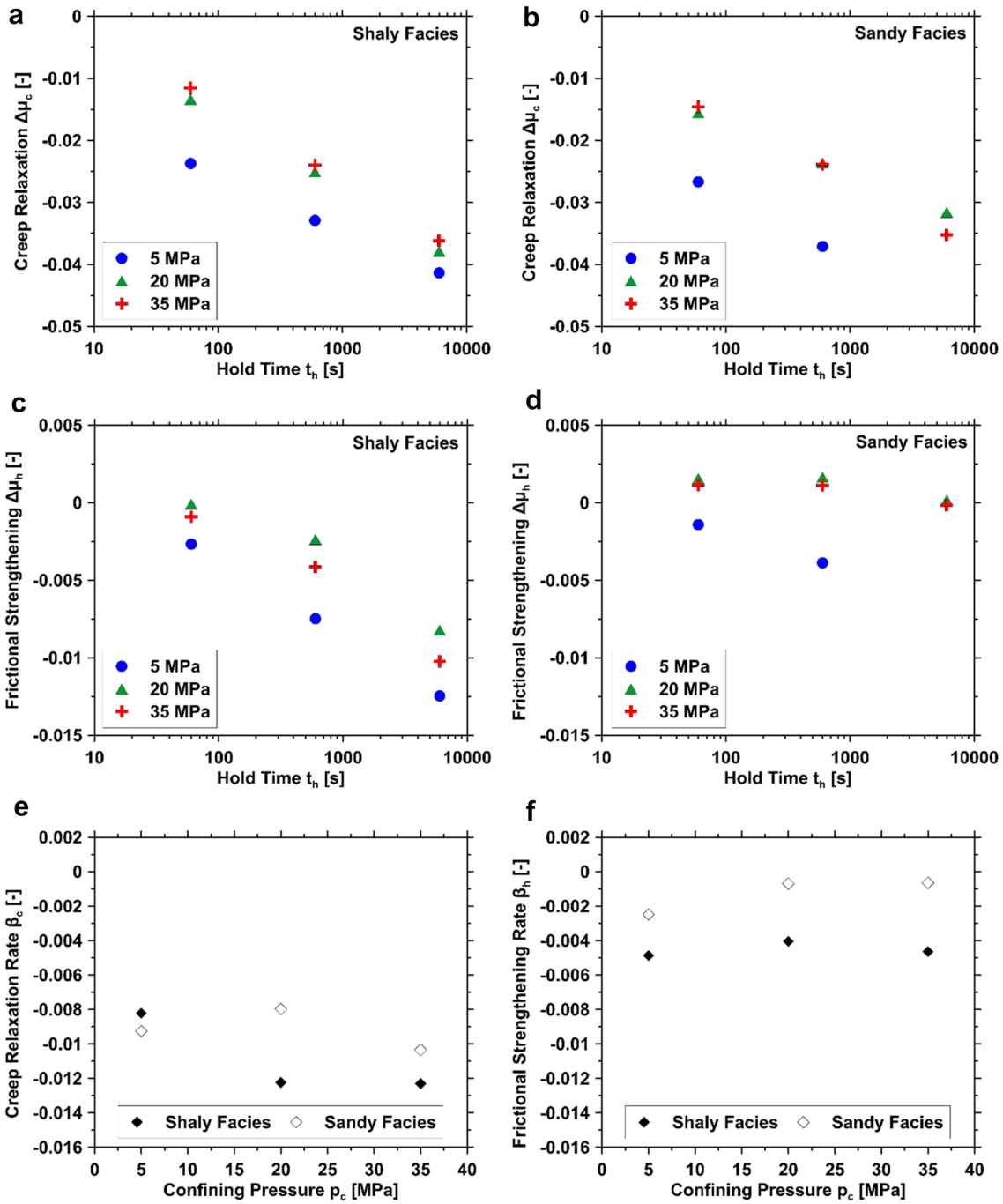

Fig. 6 Hold time versus creep relaxation $\Delta\mu_c$ (**a**, **b**) and frictional strengthening $\Delta\mu_h$ (**c**, **d**) measured during SHS tests of the shaly and sandy facies of Opalinus Clay deformed at confining pressures between 5 and 35 MPa. Resulting creep relaxation β_c (**e**) and frictional strengthening β_h (**f**) rates of both facies are shown as a function of confining pressure p_c

Subsequently, with increasing axial shortening and fault slip the velocity changes increasingly less.

At 20 and 35 MPa confining pressure, initial horizontal velocity increased slightly by about 4 m/s/MPa for the shaly facies and ~ 9 m/s/MPa for the sandy facies' samples. The increase is more pronounced for the vertical P-wave velocity (shaly facies ~ 12 m/s/MPa, sandy facies ~ 13 m/s/MPa in average). Interestingly, the $V^{B,T}_p$ (0°) progressively decreases during deformation (Fig. 8c–f). The observed velocity decrease is distinctly stronger for the sandy facies (~ 200 m/s) compared to the shaly facies (~ 20 m/s). The evolution of V_p (90°) with ongoing deformation shows the same trend as described for the experiments performed at 5 MPa confining pressure. However, the difference

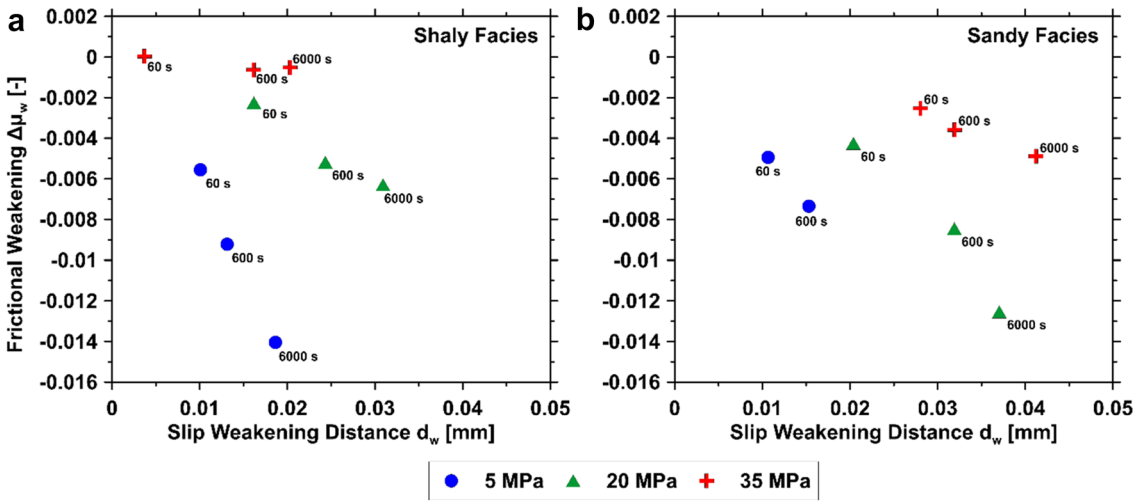

Fig. 7 Frictional weakening $\Delta\mu_w$ versus slip weakening distance d_w of the shaly (**a**) and sandy facies (**b**) of Opalinus Clay measured at re-sliding after hold periods of 60, 600 and 6000 s (indicated by numbers)

between the initial velocity and the velocity at fault reactivation increases with increasing confining pressure and is higher for the sandy (~ 200 m/s at $p_c = 20$ MPa and 280 m/s at $p_c = 35$ MPa) than for the shaly facies (150 and 200 m/s, respectively). Simultaneously, the accumulated volumetric strain prior to fault reactivation increases with increasing confining pressure. Increasing vertical velocity coincides with increasing stress and volumetric strain, except for the sandy facies at $p_c = 20$ MPa, where the volumetric strain decreases after the stress drop (Fig. 8d). This suggests that the vertical velocity increase is caused by sample bulk deformation and limited by the onset of shear displacement along the fault.

AEs were detected only during deformation tests performed on sandy facies samples. AE cumulative number increased with increasing load, depending on confining pressure and strain partitioning (Fig. 8b, d, f). At 5 MPa confining pressure, AE activity is correlated with fault sliding and starts at fault reactivation (Fig. 8b). With increasing deformation, AE activity decreased. During hold periods in SHS tests, no AEs were recorded for all specimens. However, as piston displacement resumed, AE activity simultaneously continued. With increasing confining pressure, the cumulative number of recorded AE decreased drastically (note different scales in Fig. 8). At $p_c = 20$ and 35 MPa, the onset of AE coincided with the yield stress. AE hypocenters from sandy facies samples are dominantly located along the saw-cut fault plane (see Fig. S3 of the supporting material), with the largest density of events surrounding the fault core of the sample deformed at 5 MPa confining pressure (~ 10 mm).

3.3 Deformation Structures

After each experiment, the fault surface topography of deformed samples was measured using surface profilometry. Subsequent microstructural observation of the fault topography was performed using SEM imaging of cm-sized blocks cut from one sample block. In addition, BIB-polished cross sections oriented perpendicular to the shear direction were prepared to characterize deformation structures of the interface between the fault surface and the wall rock and associated gouge development.

3.3.1 Surface Topography

In general, fault structures of deformed samples depend on confining pressure and sample facies. The roughness of the sheared fault surfaces increased compared to the starting saw-cut. Sandy facies samples display sliding surfaces that are rougher compared to the shaly facies samples deformed at similar conditions (Fig. 9). Root mean square roughness S_q also increased with increasing confining pressure. Tiny groove patterns created during sample preparation of the fault (Fig. 9a, b) were overprinted by shear deformation.

Samples of the sandy and shaly facies deformed at 5 MPa confining pressure display mating fault surfaces covered with finely pulverized wear particles (light grey colored in Fig. 9c, d). Gouge particles are distributed rather homogeneously on the surface, with several elongated topographic elevations formed by accumulated gouge. These asperities are smaller and flatter for the shaly facies, but larger and patchier for the sandy facies. Elongated heights on faults of sandy facies samples with

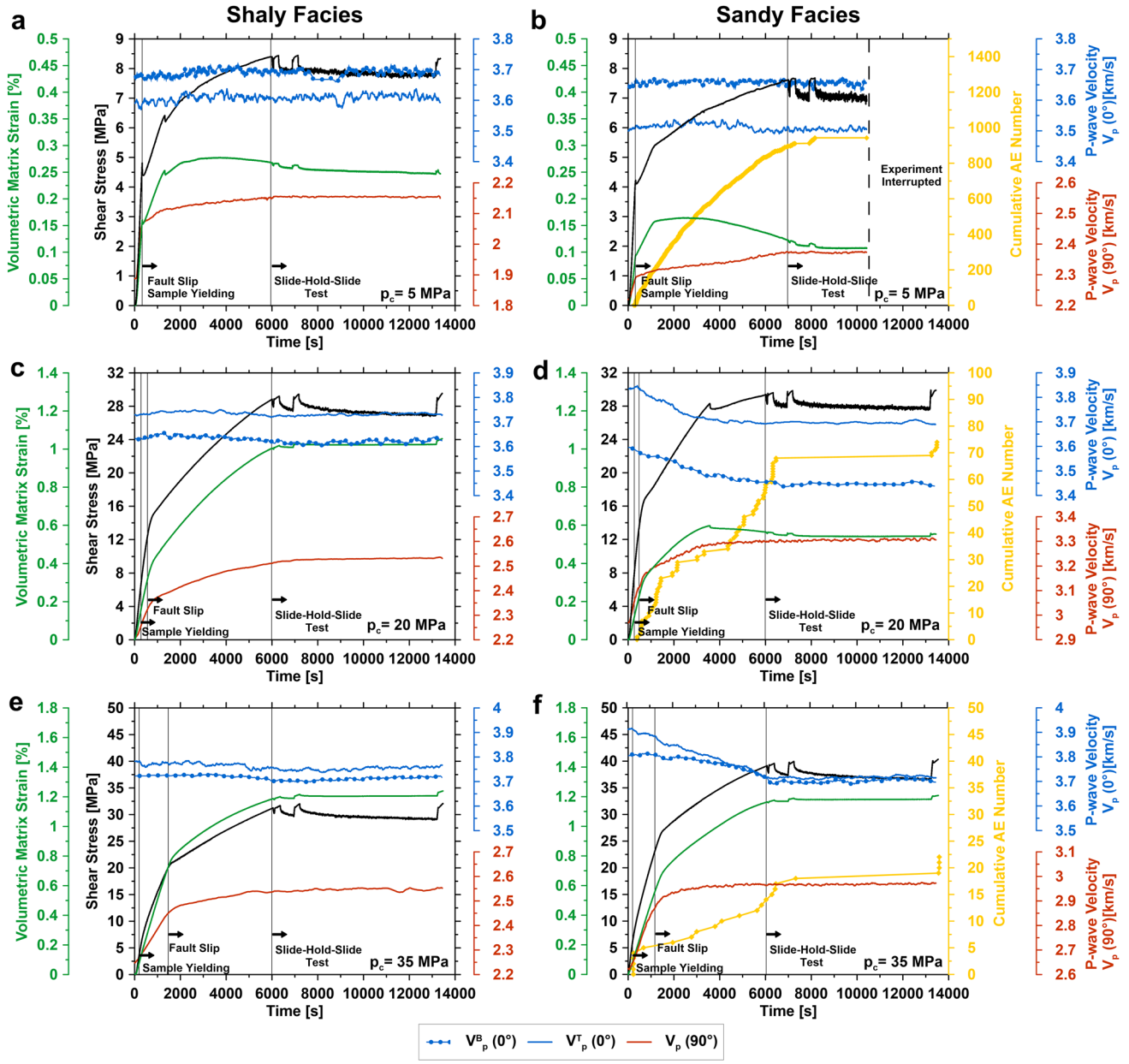

Fig. 8 Temporal evolution of shear stress (black), volumetric strain (green), cummulative acoustic emission (AE) activity (yellow) as well as horizontal (0°,bulk) and vertical (90°, crossing the saw-cut) P-wave velocity (blue and red, respectively) for the shaly (left column) and sandy facies (right column) of Opalinus Clay deformed at a confining pressure of 5 MPa (**a**, **b**), 20 MPa (**c**, **d**) and 35 MPa (**e**, **f**). Note the different scales. Vertical lines indicate sample yielding, the onset of fault slip and the start of the slide-hold-slide test protocol

their long axis oriented perpendicular to the displacement direction represent sheared sand layers of the wall rock. Topographic lows lack gouge particles and show evidence of striation characterized by grooves oriented in the sense of shear.

Gouge layers changed with increasing confining pressure depending on starting material. At confining pressures > 5 MPa slickensides developed and pulverized wear particles on the surfaces decrease gradually. Samples of the shaly facies revealed cohesive, platy, fragmented gouge, that is shinier and less pulverized at higher confining pressure (Fig. 9d, g). Topographic lows are characterized by shiny, polished, uniformly flattened and striated slickenside surfaces. Fault surfaces from sandy facies samples show the development of a stepped topography of undulating, asymmetric asperities that are elongated perpendicular to the sliding direction (Fig. 9f, h). Roughness S_q of faults from sandy facies samples was larger compared to shaly facies faults.

It is important to note that the overall surface roughness of the samples deformed at confining pressures > 5 MPa

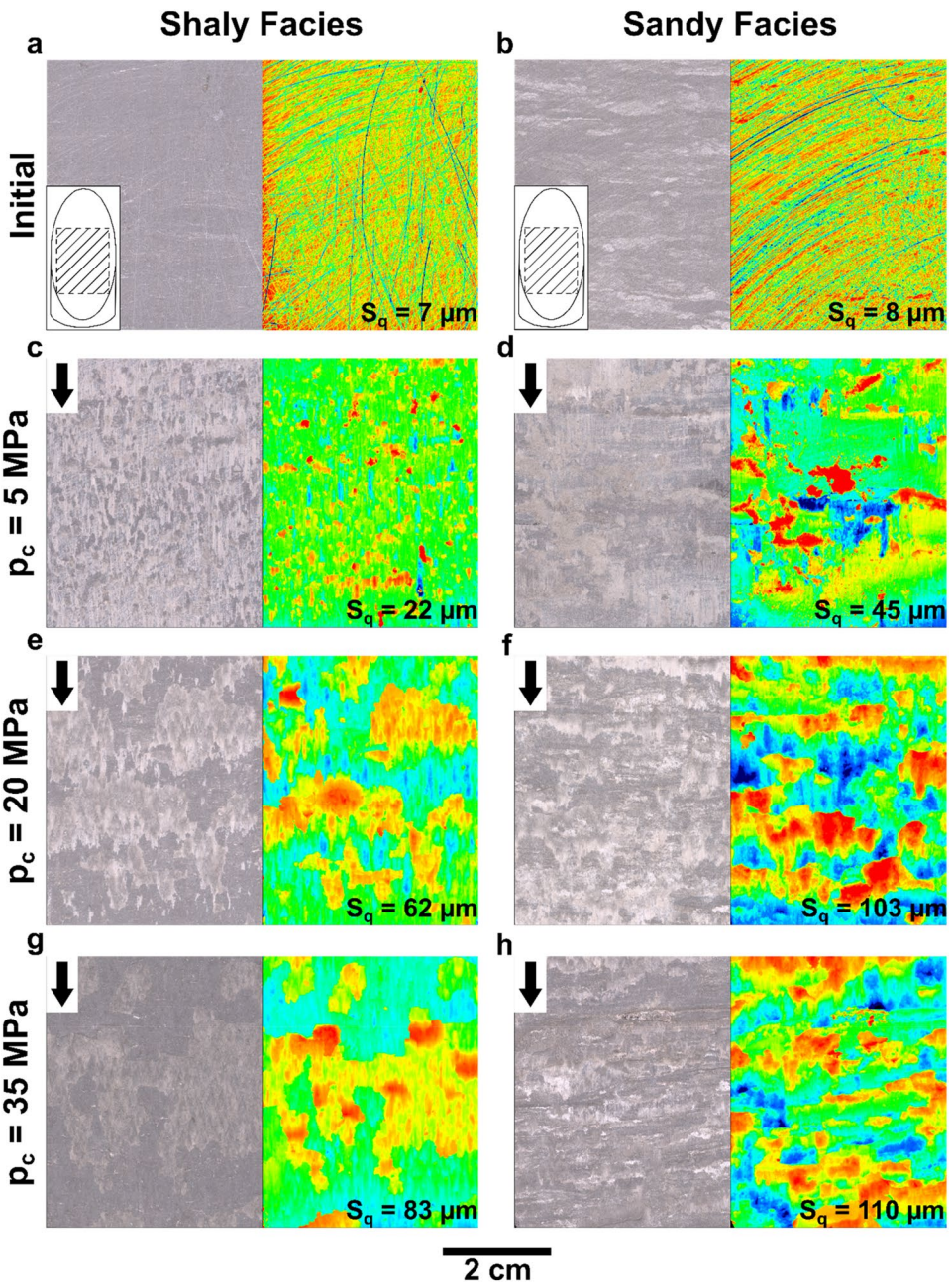

Fig. 9 Optical image of fault surface structures (footwall sample) with respective microtopography map and average RMS surface roughness S_q (measured by 3D optical profilometry) before (**a**, **b**) and after triaxial tests on Opalinus Clay at confining pressures of $p_c = 5$, 20 and 35 MPa (top to bottom). Initial roughness was in average $S_q = 7.9 \pm 2.0$ µm. Deformed samples from the shaly facies (left column) reveal smoother surfaces than those of the sandy facies (right column). The color bar on the right shows the elevation of asperities on the fault surface. Arrows indicate movement of missing block. Microtopography maps were acquired on an area of 50×40 mm^2 located at the same position for each sample (see inset in **a**, **b**)

Table 4 Root mean square (RMS) surface roughness S_q of wall rock and gouge surfaces of the shaly and sandy facies of Opalinus Clay deformed at 20 and 35 MPa confining pressure (p_c)

Opalinus Clay	$p_c = 20$ MPa		$p_c = 35$ MPa	
	S_q Wall rock (µm)	S_q Gouge (µm)	S_q Wall rock (µm)	S_q Gouge (µm)
Shaly facies	12	36	11	38
Sandy facies	26	64	26	50

p_c confining pressure

increases as larger asperities are formed by broken gouge. For these samples, we analyzed separately the topography that has been developed on the surfaces of the wall rock and gouge (Table 4). For both facies, RMS surface roughness of slickensides on the wall rock are lower than that of the gouge, and for the sandy facies the roughness of both surface types is distinctly lower compared to the complete analyzed fault surface (Fig. 9c–h). As for the whole surface (Fig. 9), the sandy facies has a higher roughness compared to the shaly facies for both types of surfaces.

Microscopic observations of the developed surface topographies are consistent down to the SEM-scale (Fig. 10).

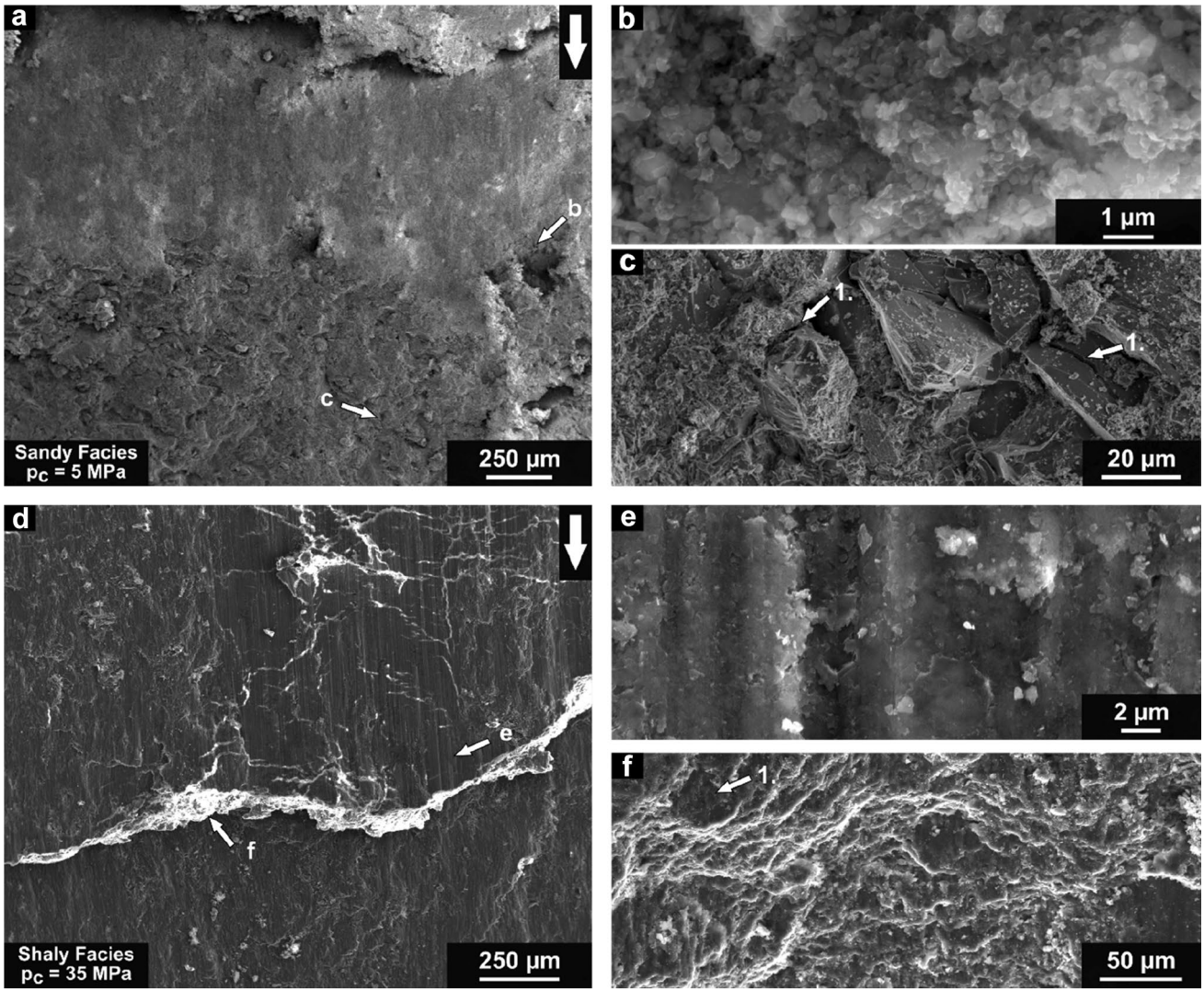

Fig. 10 SEM image of representative fault surface structures of the sandy facies (**a**) deformed at 5 MPa confining pressure. As shown in **b** at high magnification (inset of **a**), matte, pulverized wear shows an accumulation of fragmented clastic and clay minerals with a lower fabric intensity compared to slickenside surfaces. In areas with little gouge covering (**c**), clastic grains display fractures and signs of rotation in the sense of shear (inset of **a**). Fault surface of the shaly facies sample deformed at 35 MPa confining pressure (**d**) showing the development of slickensides and striations on gouge surfaces and along the boundary between the fault zone and wall rock. Polished surfaces are marked by highly laminated clay particles forming a connected smooth covering interrupted by grooves (**e**). At the edges where the cohesive gouge was broken apart after sample separation, several phyllosilicate minerals are aligned in parallel (**f**). Arrows in **a** and **d** indicate movement of the missing block

Table 5 Mineralogical composition of produced gouge after deformation of the shaly and sandy facies of Opalinus Clay at confining pressures p_c of 5–35 MPa

Opalinus Clay	p_c (MPa)	Clay (wt%)	Quartz (wt%)	Carbonates (wt%)	Feldspar (wt%)	Pyrite (wt%)
Sandy facies	5	65	24	5	6	< 1
Sandy facies	20	68	21	6	6	< 1
Sandy facies	35	66	20	4	10	< 1
Shaly facies	5	72	9	17	1	< 1
Shaly facies	20	76	8	12	3	< 1
Shaly facies	35	79	9	9	2	< 1

p_c confining pressure

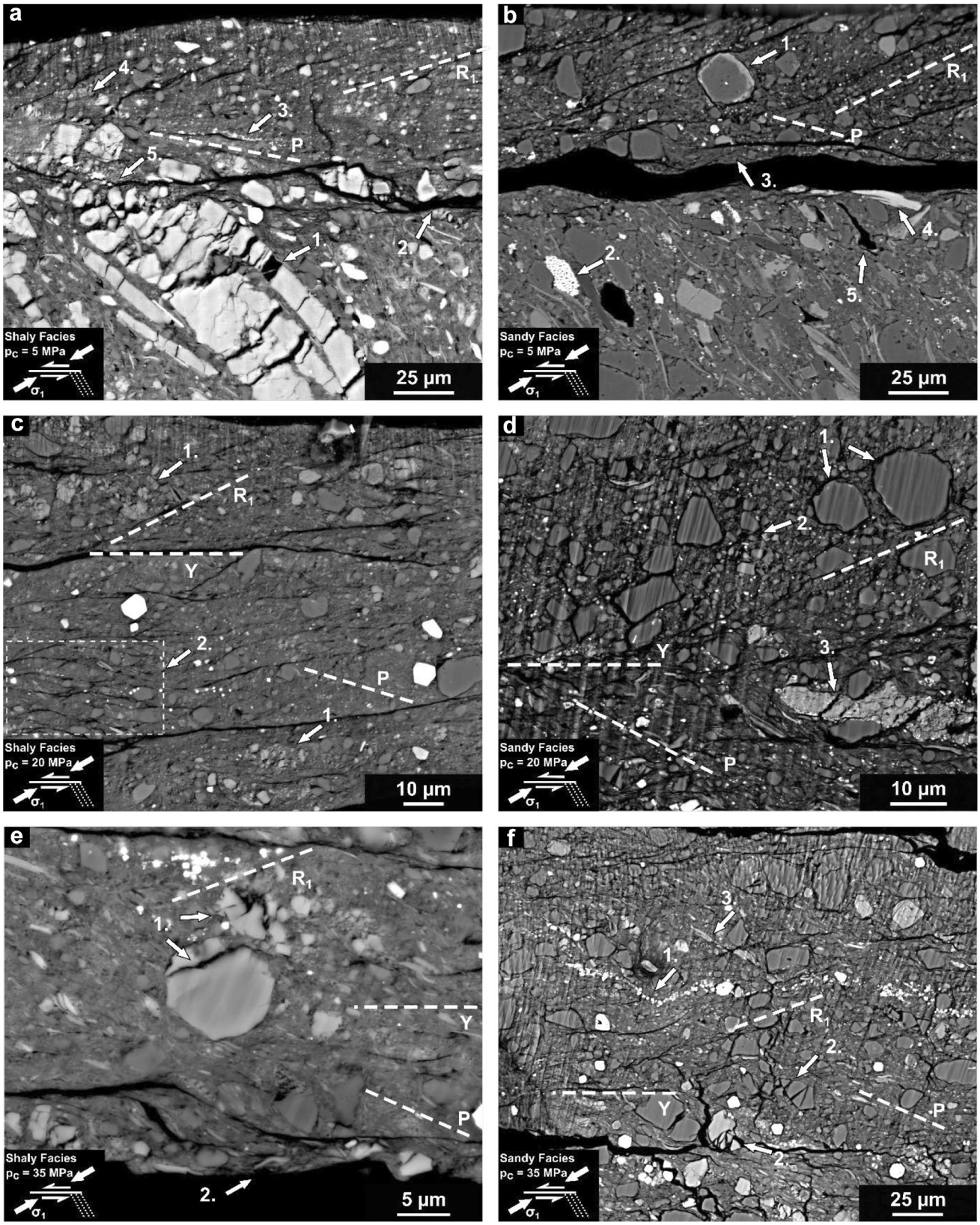
a
Shaly Facies
pC = 5 MPa
σ1
25 µm
b
Sandy Facies
pC = 5 MPa
σ1
25 µm
c
Shaly Facies
pC = 20 MPa
σ1
10 µm
d
Sandy Facies
pC = 20 MPa
σ1
10 µm
e
Shaly Facies
pC = 35 MPa
σ1
5 µm
f
Sandy Facies
pC = 35 MPa
σ1
25 µm

◂**Fig. 11** Micrographs of microstructures developed in gouge of the shaly (**a**, **c**, **e**) and sandy (**b**, **d**, **f**) facies of Opalinus Clay deformed at p_c = 5–35 MPa showing the development of several Riedel-, boundary- and Y-shear planes. Longest axis of phyllosilicate minerals preferentially aligns parallel to P-orientation. In comparison to the shaly facies, gouge development in the sandy facies is dominated by active cataclasis indicated by several broken clastic minerals and grain fragmentation. Instead, several distributed µm-thin shear zones accommodate strain in the gouge of the shaly facies with only minor cataclasis. Confining pressure, bedding plane orientation of the wall rock as well as shear and loading direction are indicated in the black boxes at the bottom left of each picture. Further details (also labeled by numbers) can be found in the text (chapter 3.3.2)

Comminuted clastic and phyllosilicate minerals forming pulverized gouge layers show grain sizes in the submicron range (Fig. 10a, b). Smooth and polished slickenside surfaces with low topography reveal a homogeneous coating of highly aligned clay particles oriented parallel to the shear surface with striations (Fig. 10d, e). We also observed an increase in gouge layer width with increasing pressures. For the sandy facies of OPA deformed at 5 MPa confining pressure, in areas with little gouge several clastic grains in sand layers of the wall rock are visible showing microcracks and rotation in the direction of slip (Fig. 10c1). At high confining pressure no comparable structures were found in both facies types. Instead, the wall rock was covered homogeneously with slickensides formed by oriented clay particles. In addition, we observed a stepped topography of multiple layers of clay minerals stacked parallel to the slip direction at the edges where the cohesive gouge was broken up after the separation of the sample halves (Fig. 10d, f). Some of these "steps" with larger exposed surface areas also show slickensides (Fig. 10f1). This suggests the development of several parallel-oriented shear planes within the fault gouge. Fault surfaces developed at 20 MPa confining pressure show transitional structures compared to samples deformed at 5 and 35 MPa.

Finally, we determined the mineralogical composition of produced gouge from all samples. To this end, a spatula was used to carefully remove the top layer of the sheared fault surface for subsequent XRD analysis (Table 5). Compared to the bulk composition of undeformed material (Table 1), gouge of the sandy facies displays a clear depletion of quartz (~21 wt%) content, whereas we observe an enrichment of clay minerals (+~30 wt%). On the other hand, there is no significant compositional difference between the bulk and gouge composition of the shaly facies.

3.3.2 Microstructural Observations of Wall Rock and Fault Interface

The gouge and damage in the adjacent host rock after deformation was observed using BIB-polished cross-sections prepared parallel to the direction of the slip and perpendicular to the fault plane. In reflected light microscopy, the gouge appears darker compared to the wall rock, probably due to grain size reduction, with occasional light-colored gouge appearing in lenses. At SEM-scale, brightness difference of these gouge lenses can be attributed to an enrichment of fragmented calcite mineral grains identified by EDX. Note that epoxy resin intruded between the gouge and wall rock interface due to the preferred orientation of particles at shear. Furthermore, SEM analysis of BIB-cross-sections reveals several microstructural elements that developed within the gouge. Following Logan et al. (1979) (see Fig. S4 of the supporting material) structures may be identified as Riedel, Y, P and boundary shear planes, which opened upon unloading but show signs of offset. We find deformation structures indicating cataclasis, frictional granular flow and intracrystalline plasticity of phyllosilicates as major acting mechanisms accommodating gouge deformation.

Structural fabric elements developed in the gouge of the two facies types are similar for each applied confining pressure (Fig. 11) with deformation microstructures generally characterized by grain size reduction of non-clay minerals, a higher fabric intensity compared to the wall rock as well as a strong shape-preferred orientation of clastic and clay minerals that distinctly differs from bedding plane orientation. The clay matrix anastomoses around clastic grains and exhibits a dominant foliation in P-orientation (sub-perpendicular to σ_1-direction), which is frequently interrupted by several R_1 and Y shears. The longest (< 150 µm), continuous R_1 shear planes formed in samples deformed at p_c = 5 MPa (Fig. 11a, b). Largest clastic particles in the gouge mostly consist of quartz and display grain sizes < 50 µm in the sandy and < 15 µm in the shaly facies samples. The sub-rounded grains show low sphericity and align parallel to clay matrix foliation (P- and R_1-shear planes). Particles in the gouge indicate a wide grain size distribution ranging from submicron to several tens of microns. Gouge layer thickness is heterogenous and a function of confining pressure and facies type revealing layers between 60 and 70 µm for samples deformed at 5 MPa confining pressure up to 200 and 280 µm for samples from sandy facies and 100 and 150 µm for shaly facies samples deformed at p_c = 20 and 35 MPa, respectively.

In gouge layers of the shaly facies of OPA (Fig. 11a, c, e), clasts are fully matrix-supported and display smaller grain sizes compared to the sandy facies (Fig. 11b, d, f). P- and Riedel shear planes may be identified by reopened fractures after unloading, revealing µm-thin shear zones with nanometer-sized clay minerals bent or aligned parallel to the local shear direction. Mineral clasts generally align with their longest axis parallel to gouge foliation. Shear zones anastomose around small clastic grains, resulting in a dense network of distributed shear planes. In both facies' types we find former framboidal pyrite (Fig. 11a3, f1) distributed along Riedel and P-shear planes as well as mica delaminated

and bent in slip direction (Fig. 11f3). Active fragmentation by cataclasis inside the gouge is indicative for calcite grains forming trails of broken clasts and spalling (Fig. 11a4, c1, e1). Fossils, which are abundant in the undeformed material and wall rock of the shaly facies, are absent in the developed gouge and have probably completely disintegrated. Samples of the shaly facies that were deformed at confining pressures of 20 and 35 MPa, reveal several Y-shears that intersect with P- and R_1-shear planes forming an undulating array of lentoid microlithons of varying size with sigmoidal-shaped shear boundaries (Fig. 11c2, e). Y-shears seem to be less abundant in gouge produced at 5 MPa confining pressure.

Gouge of sandy facies samples is characterized by a larger number of mineral clasts of different sizes, resulting in a broader grain size distribution, a more heterogeneous appearance as well as a higher porosity. Larger clasts coated with clay minerals often show particles rotated between adjacent R_1-shear planes (Fig. 11b1, d1). Furthermore, we find broken feldspar and quartz grains, which either display single fractures open subparallel to the σ_1-direction (Fig. 11d3, f2) or are highly comminuted (Fig. 11d2, f) resulting in angular fragments < 1 µm with large interparticle porosity. With progressive strain, clastic fragments may become more spherical and rounded as a result of abrasion and flaking, whereas interparticle pore space seems to decrease as clasts are reworked in the clay matrix. In sandy facies gouge, cataclasis increases with increasing confining pressure shown by an increasing amount of broken clastic grains with no or little offset as well as trails of fragmented grains. Slip also localized in R_2-shear planes in samples deformed at a confinement of 35 MPa (see Fig. S5c of the supporting material). Comparable to the shaly facies, the abundancy of Y-shears seems to be lowest at 5 MPa confining pressure. Furthermore, Y-shears seem to develop preferentially in areas of increased clay matrix content.

In the shaly facies but also in clay-rich areas of the sandy facies, gouge is bordered by very discrete, thin boundary shears (< 5 µm width) in which clay minerals align parallel to the fault surface (Fig. 11a2, b3, e2), creating a sharp contact to the bedding plane orientation of the wall rock (Fig. S5d1, S5e1). On the other hand, larger calcite grains in the shaly facies or clasts in grain-supported (sand layers) layers in the sandy facies frequently display inter- and intragranular fractures close to the gouge-wall rock boundary. The fractures are oriented sub-parallel to the σ_1-direction, indicating Mode I fracturing and stress concentration at grain contact surfaces (Fig. 11a1, Figs. S5a1, S5b1). Fractured grains often display matching grain boundaries without visible offset and apertures of several micrometers wide.

In general, and irrespective of confining pressure, the width of the damage zone adjacent to the saw-cut faults is very limited and does not exceed about 0.5 mm in sandy facies samples and is less than 0.2 mm wide in shaly facies samples. However, approaching the gouge-wall rock interface, a gradual fabric transition is sometimes indicated by fractured grains rotated towards the shear zone in sense of slip. This is shown by asymmetric opened apertures and bending and delamination of micas (Fig. 11b4, Fig. S5d1). Mineral clasts that are close to boundary shears are comminuted or flaked and dragged into the gouge (Fig. 11a5, Fig. S5a2). In the sandy facies, intergranular fractures are abundant in sand-layers, with almost undeformed clay-minerals filling the interparticle pore space (Fig. S5b3). Boundary shears pass through this porous, comminuted zone (Fig. S5b4) eroding the wall rock and supplying the gouge material. With increasing confining pressure, the thickness of the damaged zone decreases and the gouge-wall rock-interface becomes smoother and sharper (cf. Fig. S5a, Fig. S5b2, Fig. S5c1). This agrees with our macroscopic observation that the number of polished surfaces increased with increasing confinement.

Strain accumulation in the wall rock of both facies' types is indicated by pore collapse of the clay matrix, as shown by compacted clay minerals that align parallel to bedding and around larger clasts. We also found stretched organic matter and collapsed framboidal pyrite (Fig. 11b2 and 5, Figs. S5f, S5g1). With increasing confining pressure ($p_c > 5$ MPa), we observe enhanced alignment and compaction of clay platelets in the matrix as well as collapsed fossils in the shaly facies (Fig. S5g2). Sand layers in sandy facies wall rock show occasionally trans- or intergranular cracks opened sub-parallel to the maximum σ_1 stress direction. Furthermore, clay particles in the interparticle pore space of grain-supported areas show no signs of compaction (random particle orientation) in comparison to matrix-supported domains.

4 Discussion

Triaxial deformation on saw-cut samples from the shaly and sandy facies of Opalinus Clay performed at confining pressures between 5 and 35 MPa reveal a combination of elastic and inelastic deformation. Strain is partitioned between fault slip and bulk rock deformation. With increasing confining pressure, bulk deformation increases at the expense of localized fault slip. At 5 MPa pressure, all samples show brittle deformation with small stress drops initiating fault slip and subsequent shearing at almost constant shear stress. With increasing confining pressure, stress–strain curves show non-linear strain hardening without dynamic localization upon fault reactivation. Shear strength at fault reactivation increases with increasing confining pressure, whereas the friction coefficient decreases. Friction coefficients at fault reactivation of the sandy facies are slightly higher ($\mu = 0.57$

– 0.49) compared to the shaly facies ($\mu = 0.62 – 0.43$). SHS tests reveal negligible strengthening and negative or close to zero healing rates. After relaxation, stress drops upon reloading become less sharp with increasing confining pressure. At all conditions, gouge is produced and gouge layer thickness increases with confining pressure. Microstructural observations suggest a complex combination of deformation mechanisms operating concurrently. Cataclasis and brittle creep involving fragmentation and rotation of quartz, feldspar and calcite, frictional granular flow of clastic and phyllosilicate minerals grains is dominant assisted by intracrystalline plasticity of phyllosilicates. With increasing confining pressure, we observe a shift in strain partitioning from dominantly localized fault slip towards ductile deformation of the wall rock with reduced slip along the saw-cut. This is corroborated by microstructural observations in conjunction with the recorded mechanical and acoustic data. In the following, we summarize and combine the obtained experimental results to explain the observed change in the deformation behavior of faulted OPA from the sandy and shaly facies with increasing confining pressure. The results are compared to previous laboratory studies and implications for the mechanical behavior and mode of reactivation of faults in clay-rich host rocks will be discussed. Finally, deformation mechanisms during stress relaxation leading to frictional strengthening are examined to evaluate long-term stability of faults in OPA.

4.1 Fault Slip Behavior

4.1.1 Deformation Mechanisms and Behavior

For the samples deformed at 5 MPa confining pressure, we observe a rapid increase in bedding-perpendicular P-wave velocity at the beginning of axial loading (Fig. 8a, b). This indicates increasing contact area of surface asperities, resulting in better fault coupling as well as the closure of cracks and pores in the rock matrix. Compaction of bedding-parallel aligned pores has also been reported from experiments performed on intact shaly and sandy facies samples loaded perpendicular to bedding (Popp and Salzer 2007; Siegesmund et al. 2014). With further loading, the saw-cut fault starts slipping once the shear strength of the contact asperities is reached, resulting in a small stress drop. At 5 MPa confining pressure, yield stress of the bulk matrix σ_y is almost equal to the stress at reactivation σ_f. At the onset of fault slip, the slope of P-wave velocity perpendicular to bedding vs. time decreases. In sandy facies samples, the onset of fault slip is accompanied by acoustic emission activity, localizing on and near the saw-cut surface area (Fig. 8b, Fig. S3). Both observations suggest damage initiation and fragmentation of asperity contacts at the fault surface by microcracking of rigid minerals (dominating in the sandy facies) and grain rotation. In accordance with Popp and Salzer (2007) and Siegesmund et al. (2014), bedding-parallel P-wave velocity of the matrix is almost constant and increases at a much lower rate than perpendicular to it.

The concurrent increase of stress and vertical P-wave velocity at a relatively high rate indicates ongoing compaction of pore space, grain reorganization and particle rotation, presumably parallel to P-shear orientation. For both facies, the onset of brittle creep beyond yield stress is associated with strain hardening (accompanied by a second stress drop for the shaly facies sample). Matrix deformation and fault slip is accompanied by the formation of boundary and R_1-shear planes, which may contribute to the observed hardening (Haines et al. 2013). With continuing fault slip, the vertical P-wave velocity is almost constant and increases at a low, steady rate, suggesting a nearly stable microstructural configuration of the gouge. The increase in vertical P-wave velocity is likely due to gouge compaction by porosity reduction and grain fragmentation.

Axial matrix strain accounts for about 3 and 5% of the total deformation of the sandy facies and shaly facies samples, respectively. In turn, this indicates fault slip is strongly localized. This is consistent with our microstructural observations showing the formation of P- and Riedel shear planes (Fig. 11). The relatively high friction coefficients ($\mu \sim 0.85$, cf., Fig. 2e, f) and the development of incohesive and granular gouge (Fig. 9) indicate the dominance of dilatant cataclastic deformation mechanisms involving transgranular microcracking, abrasion and grain rotation of mineral grains as well as frictional sliding of phyllosilicates orienting parallel to shear planes. The observed friction coefficients are similar to commonly observed values (Byerlee 1978). Similarly, high friction coefficients (peak and residual) in the range of $\mu = 0.85$ were also reported for the shaly facies by Wild and Amann (2018) at mean effective pressures $p_c < 5$ MPa as well as for the sandy facies by Zhang and Laurich (2019) at $p_c < 25$ MPa. Also, interlayer bond strength of basal (001) planes of clay minerals increases with decreasing water content and may enhance brittle wear and abrasion (e.g., Moore and Lockner 2004; Morrow et al. 2017).

Similar to the experiments performed at 5 MPa confinement, all samples deformed at 20 and 35 MPa confining pressure show a strong initial increase in bedding-perpendicular P-wave velocity due to elastic compaction. Hardening beyond yield stress is associated with further but smaller velocity increase related to progressive closure of the saw-cut fault and compaction of bedding parallel aligned pores (Fig. 8c–f). P-wave velocity parallel to the bedding plane remains relatively constant for the shaly facies. On the other hand, bedding-parallel P-wave velocity starts decreasing more significantly above yield stress in the sandy facies (Fig. 8d, f). Fortin et al. (2006) attributed the P-wave velocity reduction in experimentally deformed sandstones to the

crushing of clastic mineral grains that dominate pore collapse and compaction. Due to the higher quartz and feldspar content of the sandy facies, damage in the bulk seems to be dominantly accommodated by microcracking, compared to the shaly facies, where pore collapse seems to dominate. This is consistent with the triaxial deformation tests on OPA performed by Popp and Salzer (2007) and Siegesmund et al. (2014), which show a higher loading-induced decrease of bedding parallel P-wave velocities for sandy compared to shaly facies. Note, that strain gauges on the upper and lower saw-cut blocks show bulk compaction in accordance with increasing axial velocity, whereas bedding-parallel P-wave velocities suggest local dilation by microcrack formation.

As no stress drop is observed at fault reactivation, we suspect developed shear fabrics to be immature and not pervasive. This may be explained by the continuing deformation of the bulk matrix at fault reactivation, resulting in low fault displacement that inhibits localized shear fabric development in the gouge but may also indicate a change of deformation mechanism towards an increasing contribution of viscous processes. The latter assumption is supported by the decrease of total acoustic emission activity (Fig. 8) in the sandy facies with increasing confining pressure as well as the generally decreasing friction coefficient of both facies (Fig. 2e, f). With increasing confining pressure, the fault contact area of the two saw-cut surfaces increases. Dilatant microfracturing of asperities is increasingly suppressed during fault slip assisting fault creep and the development of ductile shear zones as more space is needed for strain accommodation. This agrees with the findings of Moore and Lockner (2004) who suggested that clay gouge friction may decrease with increasing confining pressure due to the progressive alignment of weak (001) basal planes with shear planes. Shear-induced particle rotation close to the saw-cut surface may also enhance gouge layer thickness as a particle are incorporated into the shear zone. This may result in the development of boundary shear planes and eventually the formation of a sharp contact with the wall rock (Fig. 11, see Fig. S5). Cataclastic (grain fragmentation) and granular (grain rotation) flow with particle sliding along anastomosing µm-thin shear zones of aligned clay particles control deformation. This agrees with slickenside surfaces (Fig. 10d) that developed adjacent to gouge and wall rock in samples deformed at confining pressures > 5 MPa.

Another factor potentially contributing to the reduction of friction coefficient with increasing confining pressure is the residual water content remaining in the samples after drying at 50 °C (see chapter 2.1). Friction of clay minerals is strongly influenced by adsorbed water (e.g., Ikari et al. 2007, 2009). Given the fixed residual water content of the sandy (~0.4 wt%) and shaly (~1.0 wt%) facies, the degree of saturation depends on porosity, which closes progressively with increasing confining pressure and strain. Therefore, the degree of saturation of the samples is potentially increasing with increasing confining pressure. As a result, the reduction in friction due to clay mineral alignment and changing deformation mechanisms may be further enhanced by water-aided surface lubrication of clay minerals. Furthermore, with decreasing porosity water can fill the available pore space, which can alter the effective stress state (e.g., Saffer and Marone 2003; Ikari et al. 2007; Morrow et al. 2017).

We observe continuing strain hardening and non-linear increase of vertical P-wave velocity with progressive slip. At elevated pressures, more strain is accumulated in the bulk matrix, leading to compaction. For the shaly facies samples, we estimate 28 and 41% of total deformation being accommodated in the bulk at 20 and 35 MPa respectively. For sandy facies samples, the bulk strain is 18 and 34% at 20 and 35 MPa, respectively. In addition, hardening may result from shear-enhanced compaction involving comminution and cataclasis. Strain hardening has been associated with an increasing gouge layer thickness (Morrow et al. 2017).

Interestingly, for the sandy facies deformed at a confining pressure of 20 MPa (Fig. 8d), a stress drop was observed after ~4000 s (corresponding to a total axial strain of ~3.5%), after which the bulk strain gauges show dilatancy. Differential stress and vertical P-wave velocity continue to increase, as observed for samples deformed at 5 MPa. We posit that with shear and compaction the gouge strengthens causing abrupt localized failure, once the strength is exceeded (Baud et al. 2006). Likely, at $p_c = 35$ MPa, the pressure was sufficiently high to suppress the dilatant behavior of the matrix, which is in line with the minor increase of axial velocity (Fig. 8f). Dilatancy of the bulk is therefore an important mechanism, affecting the partitioning of the fault and matrix deformation. Due to the higher content of clastic minerals in the sandy facies, dilatant microcracking is more active in the sandy facies, whereas matrix compaction and pore collapse are more active in the clay-rich shaly facies.

Microstructure analyses of deformed samples show microfracturing, abrasion and grain rotation of clastic minerals, intracrystalline plasticity of phyllosilicates including bending, kinking and boudinage as well as frictional sliding of clay and non-clay mineral grains all contribute to sample deformation and strain localization on the saw-cut surface. The relative contribution of each mechanism to deformation depends on the mineralogic composition as well as on the applied confining pressure. Our observations suggest that grain crushing, frictional sliding and rigid body grain rotation along slip surfaces are dominant at low confining pressure in all samples. At elevated pressures strain is accommodated by cataclastic flow in the sandy facies and by granular flow in the shaly facies. Shear zone formation controlled by the frictional sliding of phyllosilicates leads to connected shear networks. Increasing contribution of cataclasis, number of undulating shear networks and gouge

layer thickness indicates continuous delocalization of strain within the developed gouge with increasing confining pressure. Therefore, the fault architecture of OPA changes with increasing confining pressure and/or decreasing overconsolidation. At 5 MPa confinement, a thin, central slip surface develops. This is in contrast to a thick, viscous shear zone produced at elevated pressures, where slip is accommodated on boundary shears at the interface between gouge and wall rock and along distributed shear planes within the gouge (cf., Fagereng and Sibson 2010). The obtained mechanical and acoustic data as well as the developed microstructures indicate a transition from brittle towards ductile deformation of OPA with increasing confining pressure at the applied conditions.

Our experimental observations show similarity to grain-scale deformation mechanisms identified in the "Main Fault" at the Mont Terri URL (Laurich et al. 2014, 2017, 2018), in particular grain size reduction by cataclasis and abrasion, frictional granular flow as well as bending of phyllosilicates. However, due to the short time scale of our experiments performed on dried sample material, other processes observed under natural conditions such as pressure solution/mineral precipitation and mineral formation (Laurich et al. 2014) are not captured. Microfabrics developed in the shaly facies samples deformed at confining pressures > 5 MPa show great similarity to the main structural elements of the "Main Fault" exposed in Mont Terri URL (cf. Laurich et al. 2014, 2017, 2018; Jaeggi et al. 2017). There, the fault gouge displays sigmoidal P-foliation (S-C fabric) and an anastomosing network of µm-thick shear zones most in Y and R_1 orientation, which is bordered by sharp Y-shears forming slickenside surfaces. Comparing the in-situ gouge fabric at Mont Terri URL, formed by faulting of a slightly overconsolidated protolith (max. burial ~ 1350 m) at an overburden of ~ 1000 m (Nussbaum et al. 2011, 2017), with the experimentally developed microfabrics, we infer ductile, aseismic deformation behavior of the "Main Fault", in agreement with field studies (Laurich et al. 2017, 2018; Hopp et al. 2022).

Interestingly, XRD analysis of sheared gouge material of the sandy facies shows a clear enrichment of the clay mineral fraction in comparison to the bulk material, suggesting a stronger incorporation of clay into the gouge material compared to the more competent sand-rich layers. These observations may have important implications for the clay smear potential (e.g., Vrolijk et al. 2016) and the sealing efficiency of fractures in the OPA sandy facies. In contrast, gouge produced in the shaly facies has a similar mineralogic composition compared to the starting material. This has also been reported for natural gouge from the "Main Fault" and the surrounding shaly facies host rock at the Mont Terri URL (Laurich et al. 2017; Wenning et al. 2021).

4.1.2 Fault Strength and Strain Localization

OPA shares deformation features of both weak rock and stiff soil (NAGRA 2002). As such, petrophysical (e.g., porosity, density) and mechanical properties (e.g., strength, compressibility and stiffness) depend on the maximum burial depth and diagenesis experienced during geological history. When a sedimentary layer is subjected to unloading after burial compaction, e.g., by geological uplift, it remains over-consolidated due to residual plastic volumetric strain. The over-consolidation ratio (OCR), expressed as the ratio of effective preconsolidation pressure to present effective vertical stress (Azizi 1999), may be used to characterize the burial history of sediment and predict its deformation behavior (Paterson and Wong 2005) when chemical cementation and horizontal tectonic compression are negligible (e.g., Ingram and Urai 1999). In the following, we discuss the obtained results in the framework of critical state theory (e.g., Cam-Clay-Model; Schofield and Wroth 1968; Roscoe and Burland 1968) and analyze volumetric strain changes in the mean effective stress ($p = (\sigma_1 + 2\ p_c)/3$) and differential stress ($\sigma_d = \sigma_1 - p_c$) space in an effort to explain the observed mode of fault reactivation and strain partitioning of the tested saw-cut samples.

In critical state models, the yielding of a porous material follows an approximately elliptically shaped, "capped" surface in the p-σ_d space, which is limited by prior normal consolidation (e.g., Schofield and Wroth 1968; Wood 1990). The yield surface expands with increasing normal consolidation or decreasing porosity, whereas elastic deformation is restricted to overconsolidated materials (Azizi 1999). It is divided by the critical state line that separates dilatant, brittle deformation including strain softening and shear localization (Hvorslev line) from compacting, ductile deformation involving strain hardening and shear-enhanced compaction (Roscoe line). With progressive shearing beyond yielding, the load path will terminate in both cases when the critical state is reached, hence when shear deformation occurs at constant volume, effective differential or mean stress, irrespective of the loading history. Describing the deformation and failure mode depending on effective stress and porosity, critical state, cap models were also applied in characterizing the constitutive behavior of several porous rocks such as sandstone, limestone, tuff and porous basalt (e.g., Scott and Nielsen 1991a, b; Wong et al. 1997; Cuss et al. 2003; Loaiza et al. 2012; Rutter and Glover 2012; Wong and Baud 2012; Nicolas et al. 2016). Failure of siliciclastic, porous rocks across the brittle-ductile transition is primarily determined by pressure-sensitive cataclastic deformation mechanisms (cf., Rutter and Hadizadeh, 1991).

For simplicity, we assume identical initial porosity of the tested samples of the shaly ($\varphi_{\text{shaly facies}} = 15.7 \pm 1.3$vol%) and the sandy facies ($\varphi_{\text{sandy facies}} = 11.1 \pm 1.1$vol%). Furthermore,

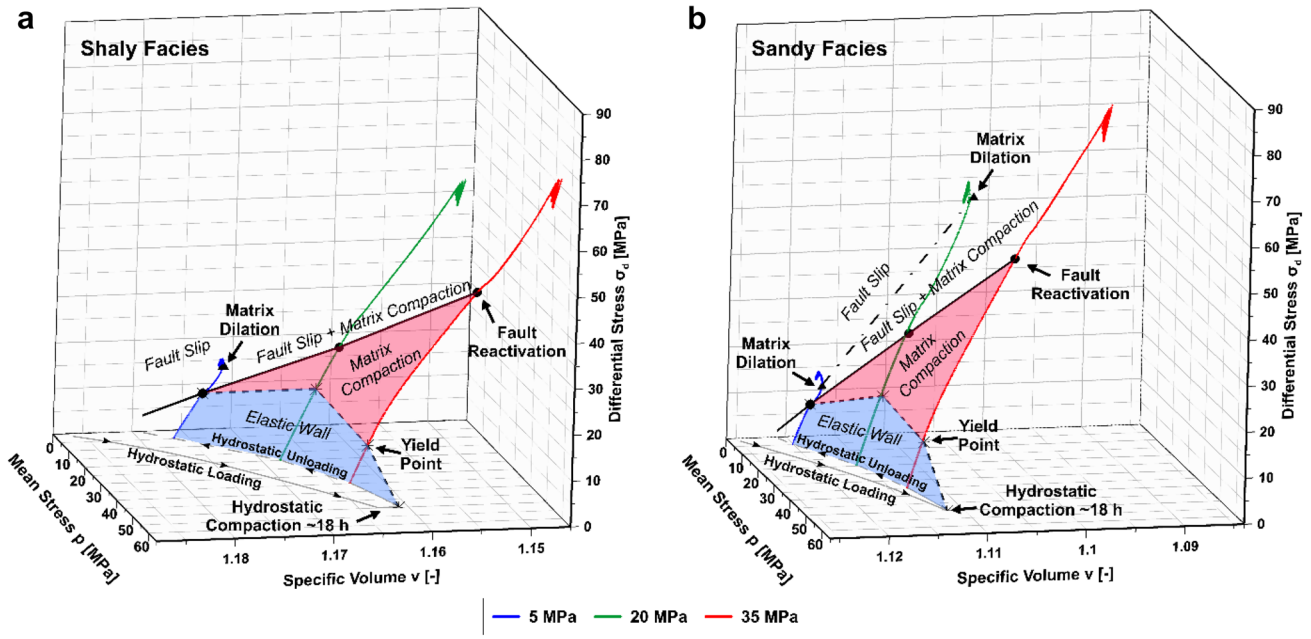

Fig. 12 Stress paths of the shaly (**a**) and sandy (**b**) facies of Opalinus Clay deformed at $p_c = 5$ (blue), 20 (green) and 35 MPa (red) projected in the three-dimensional space of mean stress – differential stress – specific volume. The use of the hydrostatic unloading curve in conjunction with the determined yield point of the bulk, fault reactivation and matrix dilation stress allowed mapping of the observed deformation modes. Stress at the onset of fault slip is indicated by black dots. Matrix dilation is indicated by black triangles

we assume that the volumetric strain measured by the strain gauges (average of SGV1/2, SGH1/2 in Fig. S1a) records a change of total porosity ($d\varphi = ((V_{sample} \times \varphi) - \varepsilon_{vol} \times V_{sample})/V_{sample}$). Following Azizi (1999), we calculated the evolution of the specific volume via the expression $v = 1 + ((\varphi - d\varphi)/(1 - (\varphi - d\varphi))$ to represent porosity changes associated with the stress path in the p-σ_d-v space (Fig. 12). We further neglect any potential pore pressure changes since the samples were dried before testing and exposed to drained boundary conditions during hydrostatic and axial deformation. Figures 12a, b show hydrostatic loading curves (solid line) of the shaly and sandy facies derived from volumetric strain measurements of the specimens deformed triaxially at a confining pressure of 35 MPa. Hydrostatic pre-compaction may represent normal consolidation (Azizi 1999) and resulted in higher volume reduction in the shaly compared to the sandy facies. During a hold phase of ~ 18 h duration at 50 MPa confining pressure, we observe creep compaction of the shaly facies and subsequent permanent specific volume reduction after unloading for both facies. Hydrostatic unloading curves (dashed line in Fig. 12) were interpolated from the final volumetric deformation obtained for each sample after reducing the confining pressure to 20 and 5 MPa, respectively. Due to the higher content of strong mineral phases (e.g., quartz, carbonates, feldspar) and lower porosity, the sandy facies generally displays higher elastic stiffness and strength parameters compared to the shaly facies, as has also been shown in previous experimental studies on OPA (cf., Popp and Salzer 2007; Gräsle and Plischke 2010, 2011; Siegesmund et al. 2014; Wild and Amann 2018; Favero et al. 2018; Zhang and Laurich 2019; Crisci et al. 2021; Schuster et al. 2021). As confining pressures were reduced for subsequent testing, samples become overconsolidated. During subsequent loading, the elastic strain component of a specific stress path depends on OCR, limited by the yield point, forming a so-called elastic wall for different stress paths (Azizi 1999). In our experiments, the elastic wall (blue area in Fig. 12) is bounded by the unloading curve in the p–v space and the yield stress of the bulk matrix. In this framework, it is assumed that the elastic wall is limited by maximum normal consolidation (Azizi 1999), which is why we extrapolated the upper limit of the wall to the p–v condition before unloading.

The differential stress paths of the tests as well as the determined yield stress and stress at fault reactivation are displayed schematically in p-σ_d-v space (Fig. 12). Elastic deformation is limited by a capped yield surface. For the specimens deformed at 5 MPa and OCR = 10, the stress at fault slip (indicated by black dots in Fig. 12) coincides with the yield stress and the upper limit of elastic matrix deformation. The release of stored elastic strain energy upon failure resulted in a stress drop (e.g., Byerlee 1970; Dieterich 1972) via stable slow slip (c.f., chapter 3.1.2). With ongoing axial shortening, deformation is first accommodated

by a combination of fault slip and matrix compaction until fault slip and dilatancy dominate (Fig. 12; blue stress path). An increase in differential stress after the onset of dilation was also observed in triaxial tests performed on full cylinder samples of OPA from both facies (e.g., Naumann et al. 2007; Amann et al. 2012; Wild and Amann 2018; Zhang and Laurich 2019; Winhausen et al. 2022), where the dilation threshold of the matrix was in the range of ~ 80–90% of peak stress. These studies also showed that dilatancy is suppressed with increasing confining pressure indicating a transition of failure mode from brittle to ductile.

For all samples deformed at confining pressures > 5 MPa, the bulk matrix yields before fault slip starts, resulting in strain-hardening matrix compaction. The stress paths (red and green paths, Fig. 12) approximately follow the Roscoe surface (red area Fig. 12). After the onset of fault slip, deformation occurs by a combination of fault slip and matrix compaction. All tested samples showed strain hardening and did not reach a critical state. This is also reflected in the gouge microstructures that evolve continuously without reaching a steady state (c.f., Haines et al. 2013; Morrow et al. 2017).

Stress at the onset of fault slip σ_f, increases linearly with increasing mean stress (Fig. 12). We use σ_f to fit a linear Mohr–Coulomb (MC) failure envelope and determine the friction coefficient at fault reactivation μ_f. In p-σ_d space, stress at fault reactivation may be expressed as $\sigma_f = a + M \times p$, where a is the intercept with the σ_d axis and M is the slope. Both parameters are transformed to the Mohr–Coulomb parameters friction angle (ϕ) and cohesion (c) using the expressions: $\phi = tan^{-1}\ \mu = sin^{-1}((3 \times M)/(6 + M))$ and $c = (a \times tan\ \phi)/M$ (Azizi 1999). Least square regression yields $M_{shaly} = 0.85$ and $M_{sandy} = 1.01$ (Table 6) corresponding to $\phi = 22°$ and 26°, respectively. The resulting friction angles ϕ correspond well to the angle of the saw-cut with the loading direction, θ (e.g., Jaeger 1960; Sibson 1985). From $\theta = 45° - \phi/2$ (Jaeger et al. 2007), we infer $\theta_{shaly} = 34°$ and $\theta_{sandy} = 32°$. The corresponding friction coefficients are $\mu_f = 0.4$ and 0.48, respectively (Table 6), in good agreement with experimentally determined sliding friction coefficients for the shaly facies of $\mu = 0.36$ obtained by Orellana et al. (2019) on dried artificial gouge of OPA. For the sandy facies, Ferrari et al. (2020) report friction coefficients at peak strength of $\mu = 0.64$–0.73 performed at $p_c \leq 1$ MPa and Orellana et al. (2020) report of $\mu = 0.38$ at a normal stress of ~ 8 MPa, both under wet conditions. The slightly higher friction coefficient of the sandy facies compared to the shaly facies maybe is related to the higher quartz content and reduced clay content of the sandy facies.

Table 6 Frictional parameters of the shaly and sandy facies of Opalinus Clay determined at fault reactivation using a linear Mohr–Coulomb failure criterion

Opalinus Clay	Fault reactivation				
	M [-]	a [MPa]	ϕ [°]	μ_f [-]	c MPa]
Shaly facies	0.85 ± 0.02	3.5 ± 0.7	22 ± 1	0.4 ± 0.01	1.7 ± 0.4
Sandy facies	1.01 ± 0.01	1.4 ± 0.2	26 ± < 1	0.48 ± < 0.01	0.6 ± 0.1

ϕ friction angle, μ_f friction coefficient at fault reactivation, c cohesion

Our experimental results demonstrate the gradual transition from brittle to ductile deformation with increasing confining pressure for OPA. Brittle, highly localized fault slip is generally present as long as matrix yield strength is similar or larger than fault strength. Once fault strength exceeds matrix yield strength, semi-brittle deformation behavior is initiated with increasing delocalization of strain, which is progressively partitioned into the wall rock. This was also observed in deformation experiments on faulted Berea sandstone (Scott and Nielsen 1991a, b) and Carrara marble (Meyer et al. 2019; Aubry et al. 2020). Meyer et al. (2019) described the influence of bulk yield stress σ_y, fault strength σ_f and matrix failure/flow stress σ_{matrix} on strain partitioning of Carrara Marble. The authors found that the relative contribution of fault slip is proportional to the stress ratio $(\sigma_f - \sigma_y)/(\sigma_{matrix} - \sigma_y)$. Therefore, the pressure at which the frictional strength of the fault exceeds bulk strength defines the brittle-ductile transition, as suggested by Byerlee (1968), giving the pressure limit for strain partitioning beyond which the fault should remain permanently locked and all strain is accommodated by diffusive matrix deformation.

To determine the pressure at the transition to ductile deformation, we compare the frictional strength of the saw-cut faults from this study with peak strength data of cylindrical samples obtained in triaxial deformation tests from several studies performed on unsaturated OPA from the shaly (water content < 6.3 wt%) and the sandy facies (water content < 4.5 wt%) deformed parallel and perpendicular to bedding orientation (Fig. 13). The data for shaly OPA are measured by Nüesch (1991) , Rummel and Weber (1999), Rummel et al. (1999) and Gräsle and Plischke (2010). Data for sandy OPA are adopted from Siegesmund et al. (2014), Zhang and Laurich (2019) and Schuster et al. (2021).

The peak strength envelope for all samples in the range of applied confining pressures may be described by non-linear failure criteria (e.g., Nüesch 1991; Naumann et al. 2007; Amann et al. 2012; Wild and Amann 2018). Assuming that the investigated range of strain rates, temperatures and water contents has no significant influence on peak strength at failure for dried samples (Schuster et al. 2021), we applied least square regression to fit the data to the empirically derived Hoek–Brown (HB) failure criterion for intact rock properties: $\sigma_1 = p_c + \sigma_{ci}\ (m_i\ (p_c/\sigma_{ci}) + 1)^{0.5}$, which relates σ_1 at peak to confining pressure p_c, uniaxial compressive strength

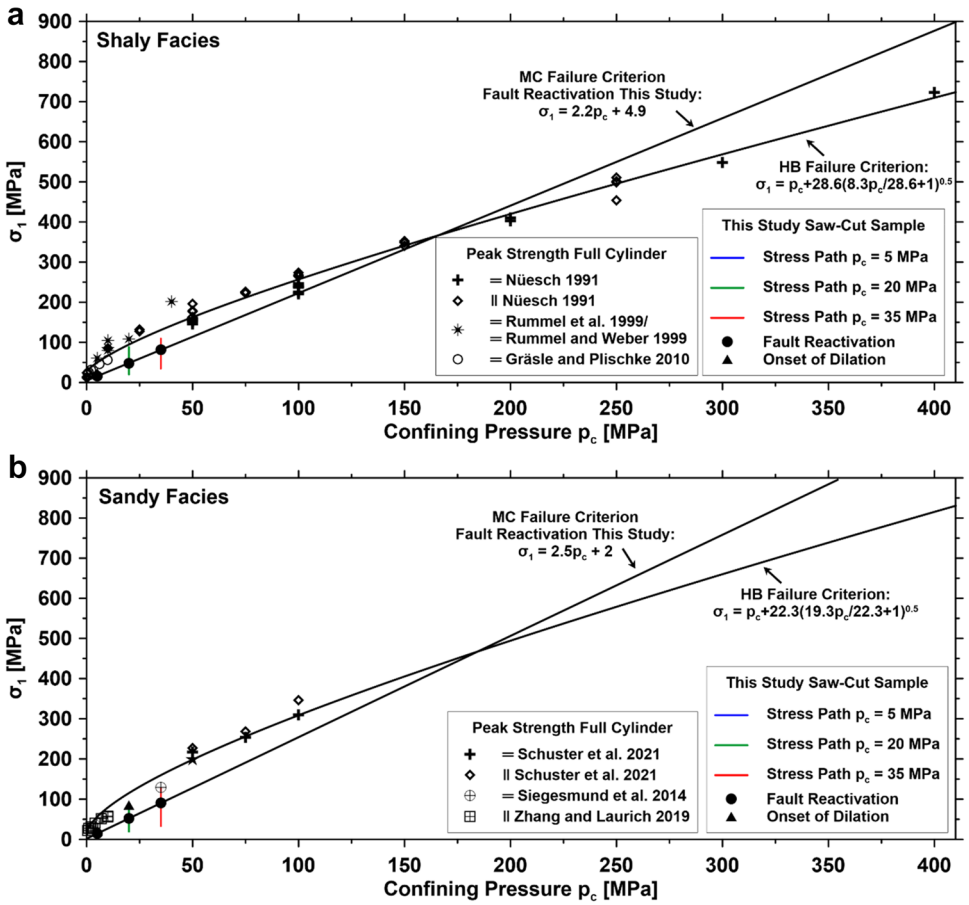

Fig. 13 Peak strength as a function of confining pressure for the shaly (**a**) and sandy facies of Opalinus Clay deformed parallel (‖) and perpendicular (=) to bedding orientation. Results of the shaly facies reported from Nüesch (1991) were obtained from samples with a water content of 1.8 wt% deformed at room temperature and strain rates of 1.3×10^{-7}–8.4×10^{-5} s^{-1}. Data selected from Rummel et al. (1999) and Rummel and Weber (1999) was limited to samples with a water content of < 2.1 wt% that were deformed at room temperature and strain rates of 10^{-6} s^{-1}. Shaly facies samples denoted as dry (water content < 6.3 wt%) by Gräsle and Plischke (2010) were also deformed at room temperature and strain rates of 10^{-6} s^{-1}. Results of the sandy facies (**b**) reported from Zhang and Laurich (2019) were obtained using samples with a water content < 3.9 wt% that were deformed at room temperature and a strain rate of 7×10^{-7} s^{-1}. Siegesmund et al. (2014) performed true triaxial experiments with $\sigma_2=\sigma_3$ at room temperature and a load rate of 0.2 MPa/min on presumably unsaturated cubic samples of the sandy facies. Experimental results from Schuster et al. (2021) were obtained at temperatures of 100 °C and strain rates of 5×10^{-4} s^{-1} using dried samples from the sandy facies with a residual water content of ~ 0.4 wt%. Peak strengths of the shaly and sandy facies were fit to a non-linear Hoek–Brown (HB) failure criterion. Furthermore, the stress at fault reactivation obtained from this study was fit to a linear Mohr–Coulomb (MC) failure criterion. The intersection of both criterions for peak strength and fault reactivation marks the transition to ductile deformation, i.e. the confining pressure at which a pre-existing fault should remain locked

(UCS) σ_{ci} and a material-specific constant m_i (Hoek and Brown 2019). Obtained m_i for shaly facies samples (Fig. 13a) corresponds well to previous work reporting $m_i=7\pm2$ for siltstones (Hoek 2007). Also, σ_{ci} agrees with UCS of unsaturated shaly facies OPA ($\sigma_{ci}=20$–25 MPa, NAGRA 2002) and/or OPA with low porosity ($\sigma_{ci}=31$–34 MPa, Jahns 2013). For the sandy facies' samples (Fig. 13b), m_i is larger compared to the shaly facies with m_i values close to those reported for sandstones ($m_i=17\pm4$; Hoek 2007).

Stress data at the onset of fault slip, σ_f, were fit with a linear MC envelope, $\sigma_f+p_c=\sigma_1=np_c+\sigma_{ci}$, where the slope n is related to μ_f by the equation $\mu_f=(n-1)/(2\sqrt{n})$ (Zoback 2007). Due to the limited data available, we assume the validity of a linear MC criterion for fault reactivation, hence constant μ_f with increasing confining pressure, and extrapolate the intersection of the fault reactivation and matrix failure envelope. We obtain a confining pressure of about $p_c=165$ MPa and $p_c=186$ MPa at the intersection for the shaly and sandy facies of OPA, respectively (Fig. 13a). Shaly facies samples become ductile at lower pressures compared to sandy facies samples in agreement with the observed difference in strength. This is likely due to the high clay content of the shaly facies.

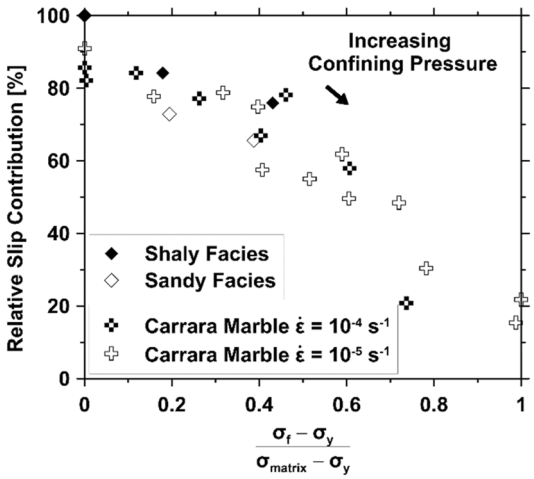

Fig. 14 Fault slip contribution to total axial shortening of the shaly and sandy facies of Opalinus Clay as a function of the ratio $(\sigma_f - \sigma_y)/(\sigma_{matrix} - \sigma_y)$ after Meyer et al. (2019). Furthermore, we compare the obtained data of Opalinus Clay with results from Meyer et al. 2019, who performed similar experiments with Carrara Marble at confining pressures $p_c = 10$–80 MPa and strain rates $\dot{\varepsilon}$ between 10^{-5} and 10^{-4} s^{-1}

Finally, we use the obtained HB-failure envelope to extrapolate σ_{matrix} for OPA and calculate the relative slip contribution, where both fault slip and matrix compaction contribute to total deformation. Following Meyer et al. (2019), we find that slip partitioning is in good agreement with the stress ratio $(\sigma_f - \sigma_y)/(\sigma_{matrix} - \sigma_y)$ (Fig. 14). As also observed by Meyer et al. (2019), we find increasing shear zone thickness with increasing confining pressure.

For OPA, our results show that brittle fault slip is expected to be promoted at high OCRs. In laboratory experiments a transition from brittle to ductile deformation behavior of weakly cemented clays, clay-rich shales as well as for OPA was found with increasing effective confining pressure, i.e. decreasing OCR towards normal consolidation (OCR = 1) (e.g., Nüesch 1991; Gutierrez et al. 1996; Nygård et al. 2006). Furthermore, increasing strength of OPA with increasing OCR and decreasing porosity was shown experimentally in triaxial and uniaxial deformation tests, performed on samples originating from different sites with varying burial and present depths (Jahns 2010, 2013; Favero et al. 2016; Ferrari et al. 2018; Crisci et al. 2019). Based on oedometer tests and basin modelling, the maximum effective burial stress of OPA at the Mont Terri site was estimated to be 17 ± 5 MPa, which results in an OCR of ~ 3–5 (NAGRA 2002; Mazurek et al. 2006). In our experimental design, we performed hydrostatic pre-conditioning up to a confining pressure of 50 MPa, aimed to minimize micro-fissures potentially introduced by preparation artefacts and sample drying. Subsequent testing at confining pressures of $p_c = 5$, 20 and 35 MPa resulted in OCRs of 10, 2.5 and 1.4, respectively. We conclude that the mode of fault reactivation depends on sedimentary burial, geological uplift and erosion.

The presented experiments were performed under dry conditions. However, fault zones in nature are barely dry and the frictional strength of clay minerals and of OPA highly depends on the degree of water saturation (e.g., Moore and Lockner 2004; Behnsen and Faulkner 2012; Morrow et al. 2017; Orellana et al. 2019). Therefore, a lower friction coefficient for the same given yield and failure envelope would increase the confining pressure where $\sigma_f < \sigma_y$, favoring brittle, highly localized fault reactivation as well as the pressure at the brittle-ductile transition where $\sigma_f > \sigma_{matrix}$ (Byerlee 1968). For saturated gouge, reactivation would probably result in a slow stable slip as shown by Orellana et al. (2018a). However, decameter, field-scale fault injection experiments of the "Main Fault" at the Mont Terri URL revealed complex slip behavior (Guglielmi et al. 2020).

4.2 Stress Relaxation and Frictional Healing

For all samples, SHS tests were started at an axial piston displacement of ~ 6 mm, i.e. an axial strain of about 6%. Total fault slip at the start of the SHS tests was different, as resolved fault slip decreased with confining pressure (Fig. 14). In general, SHS tests show minor frictional strengthening (Fig. 6c, d) and confining pressure-dependent fault slip (Fig. 7). Frictional strengthening rate in our study agrees with previous experiments performed on artificial gouge and intact samples of OPA (Orellana et al. 2018b, 2019). Generally, frictional healing arises from several time- and/or slip-dependent processes at asperity contacts and was shown to be influenced by mineral composition, temperature, pressure, presence and chemistry of pore fluids, sliding velocity, porosity, shear fabric, grainsize distribution and shape of grains (Beeler et al. 1994; Dieterich and Kilgore 1994; Hickman and Evans 1995; Karner et al. 1997; Marone 1998; Bos and Spiers 2002; Yasuhara et al. 2005; Niemeijer and Spiers 2006; Niemeijer et al. 2008; Renard et al. 2012; Carpenter et al. 2016). Following these studies, frictional strengthening of granular gouge (e.g., pure quartz or calcite mineral grains) may result from increasing compaction and fault closure by pore collapse, growth of grain contact area and increase of asperity contact strength. Pore space may be reduced by cataclasis, intercrystalline plasticity of phyllosilicates, frictional intergranular sliding and rotation (e.g., Schutjens 1991; Wong et al. 1997; Nakatani 1998; Rutter and Wanten 2000), or by time- and temperature-dependent creep accommodated by pressure solution (e.g., Bos and Spiers 2000), stress corrosion (e.g., Heap et al. 2009a, b), or dislocation activity (e.g., Renner et al. 2002).

For each hold period in the SHS runs, the piston was fixed and axial stress was allowed to relax (Figs. 4, 5). We observe

time-dependent deformation of OPA accommodated by fault slip and matrix deformation that may involve a mixture of the presented mechanisms being active along the saw-cut and/or in the matrix (depending on confining pressure). Based on our microstructural observations, we found no evidence for solution-precipitation driven compaction and contact strengthening, such as grain indentation, solution seams or mineral overgrowths, nor indicators for significant dislocation motion. Therefore, we infer that time-dependent creep during relaxation is mainly due to brittle/frictional mechanisms such as grain crushing, pore collapse and grain rearrangement caused by intercrystalline plasticity of phyllosilicates, intergranular particle sliding and microcracking.

In an ideal stress relaxation experiment using an infinite stiff loading frame, stored elastic strain energy in the specimen is dissipated through permanent deformation resulting in the decay of stress as a function of time (Guiu and Pratt 1964; Schmid 1976; Rutter and Mainprice 1978; Rutter et al. 1978). At any time during relaxation, the resulting permanent strain rate is proportional to the stress relaxation rate and depends on the rheological properties of the tested material. However, due to the compliance of the testing machine (k_m), there is an additional portion of elastic strain energy release during stress relaxation that has to be dissipated by permanent deformation in the specimen during the hold period. Therefore, during relaxation the strain rate of the specimen ($\dot{\varepsilon}_s$) is related to the stress rate ($\frac{d\sigma}{dt}$) via the expression: $\dot{\varepsilon}_s = -\left(k_m l_m + k_s\right)\frac{d\sigma}{dt}$, where k_s is the specimen compliance and l_m relates machine compliance to sample strain (Guiu and Pratt 1964).

With an emphasis on sample relaxation of 6000 s, we further characterize the different deformation behavior and the underlying acting deformation mechanisms and analyze the stress dependence of the stress relaxation rates. To determine the stress rates, stress data were first divided into 12-time intervals (1–2.5, 2.5–5, 5–10, 10–25, 25–50, 50–100, 100–250, 250–500, 500–1000, 1000–2500, 2500–5000, 5000–6000 s). Subsequently, stress rates were determined by linear fitting for the respective time intervals. Time-dependent creep may be described either by a power-law in the form of $\dot{\varepsilon}_{creep} = A(\sigma_d)^n$ or an exponential form $\dot{\varepsilon}_{creep} = Ce^{\beta\sigma_d}$ commonly used to relate creep strain rate ($\dot{\varepsilon}_{creep}$) to applied differential stress (σ_d) (e.g., Lockner 1993; Heap et al. 2009a, b; Geng et al. 2018), where the stress exponent n or the exponential law gradient β is indicative of a characteristic deformation mechanism. As shown by Schmid (1976) and Rutter et al. (1978), the stress rate in relaxation experiments can be converted into a strain rate if the machine and specimen stiffness are known. Since we could not accurately determine the relevant elastic parameters prior to the performed SHS tests, we keep the stress rate as it can be used equivalently as a proxy for the strain rate and should show identical stress dependence (Rutter et al. 1978; Rutter and Mainprice 1978).

In Fig. 15 we plot the determined stress rates to the respective differential stress during relaxation in semi-logarithmic scale. Least square fitting was applied for all determined stress rates to obtain n and β of the presented creep laws (Table 7). Obtained stress exponents range from $n = 92$ to 76 for the shaly facies and from $n = 180$ to 80 for the sandy facies and decrease with increasing applied confining pressure. The same applies to β showing higher values at low confining pressure ranging between $\beta = 4.9$–1.2 for the shaly and $\beta = 5.9$–0.9 for the sandy facies. The resulting

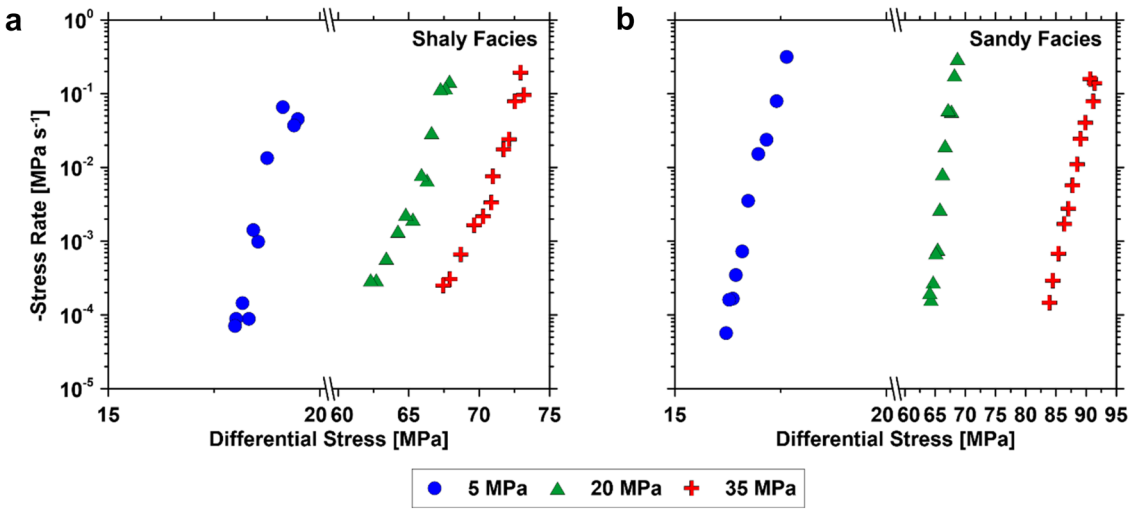

Fig. 15 Stress relaxation rate of the shaly (**a**) and sandy (**b**) facies of Opalinus Clay from SHS test at a hold period of 6000 s. Stress rate and stress data are fitted to a power-law model to obtain the slope given by the stress exponent n. Note the different and broken scales. Error bars lie within the symbol size

Table 7 Experimental conditions at the beginning of the 6000 s hold period with the regression analysis for power and exponential law that relate stress rate and differential stress during relaxation

Opalinus Clay	p_c (MPa)	σ^H_d (MPa)	n	Power law fit R^2	β	Exponential law fit R^2
Sandy facies	5	17.7	100 ± 4	0.986	5.9 ± 0.3	0.984
			104 ± 16*	0.937*	6.3 ± 0.9*	0.937*
Sandy facies	20	68.9	117 ± 5	0.980	1.8 ± 0.1	0.979
			116 ± 13*	0.939*	1.8 ± 0.2*	0.941*
Sandy facies	35	91.5	80 ± 3	0.988	0.9 ± 0.0	0.988
			80 ± 2*	0.997*	0.9 ± 0.0*	0.998*
Shaly facies	5	19.5	92 ± 11	0.898	4.9 ± 0.6	0.895
			92 ± 30*	0.697*	5.1 ± 1.7*	0.699*
Shaly facies	20	68.0	77 ± 6	0.938	1.2 ± 0.1	0.942
			56 ± 6*	0.957*	0.8 ± 0.1*	0.958*
Shaly facies	35	73.4	80 ± 6	0.955	1.1 ± 0.1	0.958
			55 ± 3*	0.989*	0.9 ± 0.1*	0.962*

The gradients n and β were determined over the full relaxation period of 6000 s (see text for details)

Gradients marked with a * were determined at hold times between 100 and 6000 s

p_c confining pressure, σ^H_d initial differential stress at the start of SHS test, R^2 correlation coefficient

stress exponents are significantly higher compared to the characteristic stress exponents ($n < 5$) for pressure solution (Rutter and Mainprice 1978; Schutjens 1991; Zhang and Spiers 2005; Zhang et al. 2010; Geng et al. 2018) or stress exponents inferred for dislocation creep in calcite or quartz (Hirth and Tullis 1992; Renner et al. 2002). Stress exponents with $n > 10$ were used to describe the brittle creep of different sandstones with $n = 20 - 70$ (Rutter and Mainprice 1978; Heap et al. 2009a, b), Tavel limestone with $n = 40–66$ (Nicolas et al. 2017), Westerly granite $n = 59–64$ (Lockner 1993) and Tournemire shale with $n = 27–63$ (Geng et al. 2018; Geng et al. 2021). These studies interpret determined stress exponents to be indicative of stress- and temperature-dependent, sub-critical crack growth by stress corrosion (Atkinson 1984) as governing deformation mechanism. Renner et al. (2000) determined stress exponents of $n = 45–110$ for shaly facies OPA specimens deformed perpendicular to bedding in creep and relaxation tests at 35 MPa confining pressure, which was also interpreted as sub-critical crack growth as the main acting deformation mechanism. Microstructural analysis indicates that stress relaxation occurs by several micromechanisms, which may act in parallel. The high-stress sensitivity in combination with microstructures may indicate dominating brittle/frictional processes such as microcracking, pore collapse, grain rotation, intergranular slip with a contribution of intercrystalline plasticity of phyllosilicates.

As described earlier, we observe continuing dilation of the shaly facies sample deformed at 5 MPa confining pressure and the sandy facies samples deformed at 5 and 20 MPa confining pressure. This suggests that the combined elastic strain of sample and machine is released by shear displacement along the saw-cut and/or gouge compaction. On the other hand, the shaly facies samples deformed at 20 and 35 MPa confining pressure and the sandy facies sample deformed at 35 MPa confining pressure show a change of axial and volumetric strain from dilation to compaction within < 1000 s. This suggests stress relaxation occurred by a combination of fault slip and matrix shortening. Therefore, we suspect that deformation in the early stage of relaxation (< 100 s) is dominated by slip along the saw-cut, which presumably decreases with increasing hold time. To investigate whether the stress sensitivity changes as soon as the dominating influence of slip decreases, we have determined n and β values as described before also for hold times > 100 s (Table 7 marked by *). We find a significant reduction of n and β for the shaly facies samples deformed at 20 and 35 MPa confining pressure, supporting our previous assumption that strain partitioning changes during a relaxation for both samples from slip to matrix compaction. On the other hand, determined gradients stay relatively constant for the remaining samples, suggesting no change in contributing deformation mechanism.

In general, our results confirm the contention from previous studies on clay-rich gouge that phyllosilicates reduce contact strengthening. Instead, clay-rich gouges may remain weak displaying stable, aseismic creep (Niemeijer et al. 2008; Tesei et al. 2012; Giorgetti et al. 2015; Carpenter et al. 2016; Ruggieri et al. 2021). However, upon reloading we find higher frictional weakening in the sandy facies compared to the shaly facies with increasing confinement. Clay-rich gouges and bulk rocks are expected to display a broad spectrum of deformation behavior related to composition and fluid content (Niemeijer and Spiers 2006; Niemeijer et al. 2010; Tesei et al. 2012; Giorgetti et al. 2015; Carpenter et al. 2016). For

example, the higher phyllosilicate content of the shaly facies samples may limit compaction at confining pressure > 5 MPa, as the intensity of shear foliation fabrics is higher compared to the sandy facies samples, allowing rapid saturation of asperity contact areas (Bos and Spiers 2000; Saffer and Marone 2003; Niemeijer and Spiers 2006; Niemeijer et al. 2008; Tesei et al. 2012; Giorgetti et al. 2015; Carpenter et al. 2016). Upon reload strain localizes in the interconnected shear surfaces developed in the shaly facies resulting in the observed stable reactivation with low frictional weakening (Niemeijer and Spiers 2006). Sandy facies samples display greater gouge heterogeneity and fraction of competent mineral clasts (e.g., quartz, carbonates) compared to the shaly facies possibly promoting frictional weakening and dilation by grain rearrangement after re-loading (cf., Fagereng and Sibson 2010). Kohli and Zoback (2013) found that a critical phyllosilicate content of less than ~ 30wt% is required for unstable frictional behavior of shale gouge. XRD-analysis of the produced gouge material of the sandy facies (Table 5) revealed much greater clay content, suggesting stable behavior. However, the heterogeneity of the sandy facies (Schuster et al. 2021) causes variations in the composition of the gouge. This may result in unstable slip patches. Finally, the amount of calcite in natural and artificial fault gouge was found to increase strength recovery (Tesei et al. 2012; Giorgetti et al. 2015; Carpenter et al. 2016; Ruggieri et al. 2021) related to increased pressure solution processes at shallow crustal conditions even at room temperature. For a fault system in OPA, this may imply higher frictional strength recovery for shear zones crossing the carbonate-rich sandy facies of OPA composed of up to 40wt% calcite (Pearson et al. 2003).

5 Conclusion

Fault reactivation, strain partitioning and frictional healing properties of saw-cut samples of OPA from the shaly and sandy facies were investigated in triaxial deformation tests. After hydrostatic pre-consolidation of 18 h at 50 MPa, constant strain rate experiments were performed at confining pressures of 5, 20 and 35 MPa at dry conditions. With increasing confinement, we observe a transition from highly localized, brittle to distributed, semi-brittle deformation behavior. At the lowest pressure, the fault slip of both facies is initiated by a small stress drop, with the subsequent strain being primarily accommodated by fault slip (> 95%). This behavior changes as pressure increases: deformation reveals non-linear strain hardening and is increasingly partitioned from stable frictional sliding towards distributed bulk deformation. The upper-pressure limit for brittle localization and the onset of strain partitioning was identified at the stress at which fault reactivation strength exceeds matrix yield stress. Shear stress at reactivation increased with increasing confining pressure. Consequently, the slip contribution to total deformation decreased with increasing confinement as yield stress and fault strength gradually diverge.

The transition in deformation behavior with confining pressure is accompanied by an increasing gouge layer thickness. Microstructural observation reveals that brittle fragmentation with frictional granular sliding and grain rotation dominate deformation at low confinement. With increasing confining pressure, we observe the formation of shear zones characterized by a higher contribution of cataclastic (sandy facies) and granular (shaly facies) flow, combined with the development of anastomosing shear plane networks, delocalizing strain within the gouge layer. AE activity during fault reactivation experiments decreased with increasing confining pressure and was only detected in sandy facies samples. Furthermore, P-wave velocity changes were more drastic in the sandy facies and became more pronounced with increasing confinement, indicating microcrack opening parallel to the stress axis and matrix compaction and pore collapse perpendicular to it.

The friction coefficient determined at fault reactivation is slightly lower for the shaly ($\mu \sim 0.4$) compared to the sandy facies ($\mu \sim 0.48$) and suggests relatively weak faults. Compared to the initial sample composition, XRD analysis of post-deformation fault gouge shows no changes in the shaly facies, but a significant depletion of quartz and enrichment of clay minerals in the sandy facies' samples, explaining the minor difference in frictional strength. Furthermore, the fractionation of clay minerals in the gouge implies increased sealing capacity of fault systems in the sandy facies. Slide-hold-slide tests (60–6000 s) performed after ~ 6 mm axial shortening reveal negative or negligible frictional strengthening of both facies indicating stable creep and long-term weakness at the applied conditions. However, sandy facies samples showed rapid frictional weakening after reload, which is why dynamic reactivation cannot be ruled out for faults in this facies type.

Our results demonstrate that the mode of fault reactivation in OPA highly depends on the sedimentary history and present stress field. Brittle fault reactivation may be favored at high overconsolidation ratios and at shallow depth increasing the risk for creating permeable flow paths and seismicity.

Supplementary Information The online version contains supplementary material available at https://doi.org/10.1007/s00603-022-03129-7.

Acknowledgements The authors acknowledge the financial support for the iCross project by the Federal Ministry of Education and Research (project number 02NUK053D), the Helmholtz Association (project number SO-093) and the GFZ German Research Centre for Geosciences Potsdam. Furthermore, Michael Naumann is highly appreciated for his technical support during the experiments. We thank

Stefan Gehrmann for sample preparation as well as Vladimir Roddatis and Anja Schreiber for assistance at the SEM. Finally, we would like to thank the editor and the two anonymous reviewers, who helped to improve the quality of this manuscript with their constructive comments and suggestions.

Funding Open Access funding enabled and organized by Projekt DEAL. Bundesministerium für Bildung und Forschung, 02NUK053D, Valerian Schuster, Helmholtz-Gemeinschaft, SO-093, Valerian Schuster.

Availability of data and material Data availability on request.

Code availability Not applicable.

Declarations

Conflict of interest The authors declare that they have no conflict of interest.

References

Amann F, Gonidec YL, Senis M, Gschwind S, Wassermann J, Nussbaum C, Sarout J (2018) Analysis of acoustic emissions recorded during a mine-by experiment in an underground research laboratory in clay shales. Int J Rock Mech Min 106:51–59. https://doi.org/10.1016/j.ijrmms.2018.04.021

Amann F, Kaiser P, Button EA (2012) Experimental study of brittle behavior of clay shale in rapid triaxial compression. Rock Mech Rock Eng 45:21–33. https://doi.org/10.1007/s00603-011-0195-9

Atkinson BK (1984) Subcritical crack growth in geological materials. J Geophys Res: Solid Earth 89:4077–4114. https://doi.org/10.1029/JB089iB06p04077

Aubry J, Passelègue FX, Escartín J, Gasc J, Deldicque D, Schubnel A (2020) Fault stability across the seismogenic zone. J Geophys Res: Solid Earth 125:e2020JB019670. https://doi.org/10.1029/2020JB019670

Azizi F (1999) Applied analyses in geotechnics. CRC Press, US

Barbour AJ (2015) Pore pressure sensitivities to dynamic strains: observations in active tectonic regions. J Geophys Res Solid Earth 120(8):5863–5883. https://doi.org/10.1002/2015JB012201

Baud P, Vajdova V, Wong T-f (2006) Shear-enhanced compaction and strain localization: inelastic deformation and constitutive modeling of four porous sandstones. J Geophys Res: Solid Earth. https://doi.org/10.1029/2005JB004101

Beeler NM, Tullis TE, Weeks JD (1994) The roles of time and displacement in the evolution effect in rock friction. Geophys Res Lett 21:1987–1990. https://doi.org/10.1029/94GL01599

Behnsen J, Faulkner DR (2012) The effect of mineralogy and effective normal stress on frictional strength of sheet silicates. J Struct Geol 42:49–61. https://doi.org/10.1016/j.jsg.2012.06.015

Bos B, Spiers CJ (2000) Effect of phyllosilicates on fluid-assisted healing of gouge-bearing faults. Earth Planet Sc Lett 184:199–210. https://doi.org/10.1016/S0012-821X(00)00304-6

Bos B, Spiers CJ (2002) Fluid-assisted healing processes in gouge-bearing faults: insights from experiments on a rock analogue system. Pure Appl Geophys 159:2537–2566. https://doi.org/10.1007/s00024-002-8747-2

Bossart P, Milnes AG (2017) Mont Terri rock laboratory, 20 years of research. Swiss J Geosci 110:1–411. https://doi.org/10.1007/978-3-319-70458-6

Bourg IC (2015) Sealing shales versus brittle shales: a sharp threshold in the material properties and energy technology uses of fine-grained sedimentary rocks. Environ Sci Technol Lett 2:255–259. https://doi.org/10.1021/acs.estlett.5b00233

Bullock RJ, De Paola N, Holdsworth RE (2015) An experimental investigation into the role of phyllosilicate content on earthquake propagation during seismic slip in carbonate faults. J Geophys Res: Solid Earth 120:3187–3207. https://doi.org/10.1002/2015JB011914

Byerlee JD (1968) Brittle-ductile transition in rocks. J Geophys Res 1896–1977(73):4741–4750. https://doi.org/10.1029/JB073i014p04741

Byerlee JD (1970) The mechanics of stick-slip. Tectonophysics 9:475–486. https://doi.org/10.1016/0040-1951(70)90059-4

Byerlee JD (1978) Friction of rocks. Pure Appl Geophys 116:615–626. https://doi.org/10.1007/BF00876528

Carpenter BM, Ikari MJ, Marone C (2016) Laboratory observations of time-dependent frictional strengthening and stress relaxation in natural and synthetic fault gouges. J Geophys Res: Solid Earth 121:1183–1201. https://doi.org/10.1002/2015JB012136

Collettini C, Niemeijer A, Viti C, Marone C (2009a) Fault zone fabric and fault weakness. Nature 462:907–910. https://doi.org/10.1038/nature08585

Collettini C, Viti C, Smith SAF, Holdsworth RE (2009b) Development of interconnected talc networks and weakening of continental low-angle normal faults. Geology 37:567–570. https://doi.org/10.1130/G25645A.1

Collettini C, Tesei T, Scuderi MM, Carpenter BM, Viti C (2019) Beyond Byerlee friction, weak faults and implications for slip behavior. Earth Planet Sc Lett 519:245–263. https://doi.org/10.1016/j.epsl.2019.05.011

Corkum AG, Martin CD (2007) The mechanical behaviour of weak mudstone (Opalinus Clay) at low stresses. Int J Rock Mech Min 44:196–209. https://doi.org/10.1016/j.ijrmms.2006.06.004

Crawford BR, Faulkner DR, Rutter EH (2008) Strength, porosity, and permeability development during hydrostatic and shear loading of synthetic quartz-clay fault gouge. J Geophysical Res: Solid Earth. https://doi.org/10.1029/2006jb004634

Crisci E, Ferrari A, Giger SB, Laloui L (2019) Hydro-mechanical behaviour of shallow Opalinus Clay shale. Eng Geol 251:214–227. https://doi.org/10.1016/j.enggeo.2019.01.016

Crisci E, Ferrari A, Giger SB, Laloui L (2021) Effect of the mineralogical composition on the elastoplastic hydromechanical response of Opalinus Clay shale. Int J Rock Mech Min 143:104747. https://doi.org/10.1016/j.ijrmms.2021.104747

Cuss RJ, Rutter EH, Holloway RF (2003) The application of critical state soil mechanics to the mechanical behaviour of porous sandstones. Int J Rock Mech Min 40:847–862. https://doi.org/10.1016/S1365-1609(03)00053-4

den Hartog SAM, Niemeijer AR, Spiers CJ (2012a) New constraints on megathrust slip stability under subduction zone P-T conditions.

Earth Planet Sc Lett 353–354:240–252. https://doi.org/10.1016/j.epsl.2012.08.022
den Hartog SAM, Peach CJ, de Winter DAM, Spiers CJ, Shimamoto T (2012b) Frictional properties of megathrust fault gouges at low sliding velocities: new data on effects of normal stress and temperature. J Struct Geol 38:156–171. https://doi.org/10.1016/j.jsg.2011.12.001
Dieterich JH (1972) Time-dependent friction in rocks. J Geophys Res 1896–1977(77):3690–3697. https://doi.org/10.1029/JB077i020p03690
Dieterich JH, Kilgore BD (1994) Direct observation of frictional contacts: new insights for state-dependent properties. Pure Appl Geophys 143:283–302. https://doi.org/10.1007/BF00874332
Doebelin N, Kleeberg R (2015) Profex: a graphical user interface for the Rietveld refinement program BGMN. J Appl Crystallogr 48:1573–1580. https://doi.org/10.1107/S1600576715014685
Fagereng Å, Sibson RH (2010) Mélange rheology and seismic style. Geology 38:751–754. https://doi.org/10.1130/G30868.1
Faulkner DR, Lewis AC, Rutter EH (2003) On the internal structure and mechanics of large strike-slip fault zones: field observations of the Carboneras fault in southeastern Spain. Tectonophysics 367:235–251. https://doi.org/10.1016/S0040-1951(03)00134-3
Faulkner DR, Mitchell TM, Behnsen J, Hirose T, Shimamoto T (2011) Stuck in the mud? Earthquake nucleation and propagation through accretionary forearcs. Geophys Res Lett. https://doi.org/10.1029/2011GL048552
Favero V, Ferrari A, Laloui L (2016) On the hydro-mechanical behaviour of remoulded and natural Opalinus Clay shale. Eng Geol 208:128–135. https://doi.org/10.1016/j.enggeo.2016.04.030
Favero V, Ferrari A, Laloui L (2018) Anisotropic behaviour of Opalinus Clay through consolidated and drained triaxial testing in saturated conditions. Rock Mech Rock Eng 51:1305–1319. https://doi.org/10.1007/s00603-017-1398-5
Ferrari A, Crisci A, Laloui L (2018) Geotechnical experimental characterization of Opalinus clay cores from the Borehole Lausen, vol Nagra Arbeitsbericht NAB 17–27. Nagra, Wettingen, Switzerland
Ferrari A, Rosone M, Ziccarelli M, Giger SB (2020) The shear strength of Opalinus Clay shale in the remoulded state. Geomech Energy Envir 21:100142. https://doi.org/10.1016/j.gete.2019.100142
Font Y, Kao H, Lallemand S, Liu C-S, Chiao L-Y (2004) Hypocentre determination offshore of eastern Taiwan using the Maximum Intersection method. Geophys J Int 158:655–675. https://doi.org/10.1111/j.1365-246X.2004.02317.x
Fortin J, Stanchits S, Dresen G, Guéguen Y (2006) Acoustic emission and velocities associated with the formation of compaction bands in sandstone. J Geophys Res: Solid Earth. https://doi.org/10.1029/2005JB003854
Geng Z et al (2018) Time and temperature dependent creep in Tournemire Shale. J Geophys Res: Solid Earth 123:9658–9675. https://doi.org/10.1029/2018JB016169
Geng Z, Bonnelye A, David C, Dick P, Wang Y, Schubnel A (2021) Pressure solution compaction during creep deformation of Tournemire Shale: implications for temporal sealing in shales. J Geophys Res: Solid Earth 126:e2020JB021370. https://doi.org/10.1029/2020JB021370
Gens A, Vaunat J, Garitte B, Wileveau Y (2007) In situ behaviour of a stiff layered clay subject to thermal loading: observations and interpretation. Geotechnique 57:207–228. https://doi.org/10.1680/geot.2007.57.2.207
Ghabezloo S, Sulem J (2009) Stress dependent thermal pressurization of a fluid-saturated rock. Rock Mech Rock Eng 42:1–24. https://doi.org/10.1007/s00603-008-0165-z
Giorgetti C, Carpenter BM, Collettini C (2015) Frictional behavior of talc-calcite mixtures. J Geophys Res: Solid Earth 120:6614–6633. https://doi.org/10.1002/2015JB011970
Goebel THW, Becker TW, Sammis CG, Dresen G, Schorlemmer D (2014) Off-fault damage and acoustic emission distributions during the evolution of structurally complex faults over series of stick-slip events. Geophys J Int 197:1705–1718. https://doi.org/10.1093/gji/ggu074
Gräsle W, Plischke I (2010) LT Experiment: mechanical behaviour of Opalinus Clay, Final Report from Phase 6–14. Mont Terri Technical Report 2009-07
Gräsle W, Plischke I (2011) LT-A Experiment: mechanical behavior of Opalinus Clay, Data report from Phase 15. Mont Terri Technical Note TN 2010-86
Guglielmi Y, Birkholzer J, Rutqvist J, Jeanne P, Nussbaum C (2017) Can fault leakage occur before or without reactivation? Results from an in situ fault reactivation experiment at Mont Terri. Energy Procedia 114:3167–3174. https://doi.org/10.1016/j.egypro.2017.03.1445
Guglielmi Y, Nussbaum C, Jeanne P, Rutqvist J, Cappa F, Birkholzer J (2020) Complexity of fault rupture and fluid leakage in shale: insights from a controlled fault activation experiment. J Geophys Res: Solid Earth 125:e2019JB017781. https://doi.org/10.1029/2019JB017781
Guglielmi Y, Nussbaum C, Cappa F, De Barros L, Rutqvist J, Birkholzer J (2021) Field-scale fault reactivation experiments by fluid injection highlight aseismic leakage in caprock analogs: Implications for CO2 sequestration. Int J Greenh Gas Con 111:103471. https://doi.org/10.1016/j.ijggc.2021.103471
Guiu F, Pratt PL (1964) Stress relaxation and the plastic deformation of solids. Phys Status Solidi 6:111–120. https://doi.org/10.1002/pssb.19640060108
Gutierrez M, Vik G, Berre T (1996) Shale strength as function of stress history and diagenesis. In: ISRM International Symposium - EUROCK 96, 1996. ISRM-EUROCK-1996–010
Haines SH, Kaproth B, Marone C, Saffer D, van der Pluijm B (2013) Shear zones in clay-rich fault gouge: a laboratory study of fabric development and evolution. J Struct Geol 51:206–225. https://doi.org/10.1016/j.jsg.2013.01.002
Heap MJ, Baud P, Meredith PG (2009a) Influence of temperature on brittle creep in sandstones. Geophys Res Lett. https://doi.org/10.1029/2009GL039373
Heap MJ, Baud P, Meredith PG, Bell AF, Main IG (2009b) Time-dependent brittle creep in Darley Dale sandstone. J Geophys Res: Solid Earth. https://doi.org/10.1029/2008JB006212
Hickman SH, Evans B (1995) Kinetics of pressure solution at halite-silica interfaces and intergranular clay films. J Geophys Res 100:13113–13132. https://doi.org/10.1029/95JB00911
Hirth G, Tullis J (1992) Dislocation creep regimes in quartz aggregates. J Struct Geol 14:145–159. https://doi.org/10.1016/0191-8141(92)90053-Y
Hoek E (2007) Practical rock engineering: RocScience. Available from the publisher at http://www.rocscience.com/hoek/PracticalRockEngineering.asp
Hoek E, Brown ET (2019) The Hoek-Brown failure criterion and GSI – 2018 edition. J Rock Mech Geotech 11:445–463. https://doi.org/10.1016/j.jrmge.2018.08.001
Hopp C et al (2022) The effect of fault architecture on slip behavior in shale revealed by distributed fiber optic strain sensing. J Geophys Res: Solid Earth 127:e2021JB022432. https://doi.org/10.1029/2021JB022432
Hostettler B et al (2017) Litho- and biostratigraphy of the Opalinus Clay and bounding formations in the Mont Terri rock laboratory (Switzerland). Swiss J Geosci 110:23–37. https://doi.org/10.1007/s00015-016-0250-3
Houben ME, Desbois G, Urai JL (2013) Pore morphology and distribution in the Shaly facies of Opalinus Clay (Mont Terri, Switzerland): insights from representative 2D BIB–SEM investigations

on mm to nm scale. Appl Clay Sci 71:82–97. https://doi.org/10.1016/j.clay.2012.11.006

Houben ME, Desbois G, Urai JL (2014) A comparative study of representative 2D microstructures in Shaly and Sandy facies of Opalinus Clay (Mont Terri, Switzerland) inferred form BIB-SEM and MIP methods. Mar Petrol Geol 49:143–161. https://doi.org/10.1016/j.marpetgeo.2013.10.009

Ikari MJ, Saffer DM, Marone C (2007) Effect of hydration state on the frictional properties of montmorillonite-based fault gouge. J Geophys Res: Solid Earth. https://doi.org/10.1029/2006JB004748

Ikari MJ, Saffer DM, Marone C (2009) Frictional and hydrologic properties of clay-rich fault gouge. J Geophys Res: Solid Earth. https://doi.org/10.1029/2008JB006089

Ingram GM, Urai JL (1999) Top-seal leakage through faults and fractures: the role of mudrock properties. Geol Society, Lond, Spec Publ 158:125–135

Jaeger JC (1960) Shear failure of anistropic rocks. Geol Mag 97:65–72. https://doi.org/10.1017/S0016756800061100

Jaeger JC, Cook NGW, Zimmerman RW (2007) Fundamentals of rock mechanics, 4th edn. Blackwell, Malden, Mass, Oxford

Jaeggi D, Laurich B, Nussbaum C, Schuster K, Connolly P (2017) Tectonic structure of the main fault in the Opalinus Clay, Mont Terri rock laboratory (Switzerland). Swiss J Geosci 110:67–84. https://doi.org/10.1007/s00015-016-0243-2

Jahns E (2010) RA Experiment: Opalinus Clay rock characterization. Mont Terri technical note 2008-55 rev

Jahns E (2013) Geomechanical laboratory tests on Opalinus Clay cores from the borehole Schlattingen SLA-1. vol Nagra Arbeitsbericht NAB 13–18. Nagra, Wettingen, Switzerland

Karner SL, Marone C, Evans B (1997) Laboratory study of fault healing and lithification in simulated fault gouge under hydrothermal conditions. Tectonophysics 277:41–55. https://doi.org/10.1016/S0040-1951(97)00077-2

Kneuker T, Furche M (2021) Capturing the structural and compositional variability of Opalinus Clay: constraints from multidisciplinary investigations of Mont Terri drill cores (Switzerland). Environ Earth Sci 80:421. https://doi.org/10.1007/s12665-021-09708-1

Kohli AH, Zoback MD (2013) Frictional properties of shale reservoir rocks. J Geophys Res: Solid Earth 118:5109–5125. https://doi.org/10.1002/jgrb.50346

Kwiatek G, Goebel THW, Dresen G (2014) Seismic moment tensor and b value variations over successive seismic cycles in laboratory stick-slip experiments. Geophys Res Lett 41:5838–5846. https://doi.org/10.1002/2014GL060159

Lauper B, Jaeggi D, Deplazes G, Foubert A (2018) Multi-proxy facies analysis of the Opalinus Clay and depositional implications (Mont Terri rock laboratory, Switzerland). Swiss J Geosci 111:383–398. https://doi.org/10.1007/s00015-018-0303-x

Lauper B, Zimmerli GN, Jaeggi D, Deplazes G, Wohlwend S, Rempfer J, Foubert A (2021) Quantification of lithological heterogeneity within Opalinus Clay: toward a uniform subfacies classification scheme using a novel automated core image recognition tool. Front Earth Sci. https://doi.org/10.3389/feart.2021.645596

Laurich B, Urai JL, Desbois G, Vollmer C, Nussbaum C (2014) Microstructural evolution of an incipient fault zone in Opalinus Clay: Insights from an optical and electron microscopic study of ion-beam polished samples from the main fault in the Mt-Terri underground research laboratory. J Struct Geol 67:107–128. https://doi.org/10.1016/j.jsg.2014.07.014

Laurich B, Urai JL, Nussbaum C (2017) Microstructures and deformation mechanisms in Opalinus Clay: insights from scaly clay from the main fault in the Mont Terri rock laboratory (CH). Solid Earth 8:27–44. https://doi.org/10.5194/se-8-27-2017

Laurich B, Urai JL, Vollmer C, Nussbaum C (2018) Deformation mechanisms and evolution of the microstructure of gouge in the main fault in Opalinus Clay in the Mont Terri rock laboratory (CH). Solid Earth 9:1–24. https://doi.org/10.5194/se-9-1-2018

Lisjak A, Garitte B, Grasselli G, Müller HR, Vietor T (2015) The excavation of a circular tunnel in a bedded argillaceous rock (Opalinus Clay): short-term rock mass response and FDEM numerical analysis. Tunn Undergr Space Technol 45:227–248. https://doi.org/10.1016/j.tust.2014.09.014

Loaiza S, Fortin J, Schubnel A, Gueguen Y, Vinciguerra S, Moreira M (2012) Mechanical behavior and localized failure modes in a porous basalt from the Azores. Geophys Res Lett. https://doi.org/10.1029/2012GL053218

Lockner D (1993) Room temperature creep in saturated granite. J Geophys Res: Solid Earth 98:475–487. https://doi.org/10.1029/92JB01828

Logan JM, Rauenzahn KA (1987) Frictional dependence of gouge mixtures of quartz and montmorillonite on velocity, composition and fabric. Tectonophysics 144:87–108

Logan JM, Freiedman M, Higgs N, Dengo C, Shimamoto T (1979) Experimental studies of simulated gouge and their application to studies of natural fault zones. Proceedings of Conference VIII on analysis of actual fault zones in Bedrock US Geological Survey, Open File Report, pp 79–1239

Marone C (1998) Laboratory-derived friction laws and their application to seismic faulting. Annu Rev Earth Planet Sci 26:643–696. https://doi.org/10.1146/annurev.earth.26.1.643

Mazurek M, Hurford AJ, Leu W (2006) Unravelling the multi-stage burial history of the Swiss Molasse Basin: integration of apatite fission track, vitrinite reflectance and biomarker isomerisation analysis. Basin Res 18:27–50. https://doi.org/10.1111/j.1365-2117.2006.00286.x

Mazzoldi A, Rinaldi AP, Borgia A, Rutqvist J (2012) Induced seismicity within geological carbon sequestration projects: maximum earthquake magnitude and leakage potential from undetected faults. Int J Greenh Gas Con 10:434–442. https://doi.org/10.1016/j.ijggc.2012.07.012

Meyer GG, Brantut N, Mitchell TM, Meredith PG (2019) Fault reactivation and strain partitioning across the brittle-ductile transition. Geology 47:1127–1130. https://doi.org/10.1130/G46516.1

Moore DE, Lockner DA (2004) Crystallographic controls on the frictional behavior of dry and water-saturated sheet structure minerals. J Geophys Res: Solid Earth. https://doi.org/10.1029/2003jb002582

Morrow CA, Moore DE, Lockner DA (2017) Frictional strength of wet and dry montmorillonite. J Geophys Res: Solid Earth 122:3392–3409. https://doi.org/10.1002/2016JB013658

NAGRA (2002) Projekt Opalinuston - synthese der geowissenschaftlichen Untersuchungsergebnisse. vol NTB 02-03. Technical report of the national cooperative for the disposal of radioactive waste. Nagra, Wettingen, Switzerland

Nakatani M (1998) A new mechanism of slip weakening and strength recovery of friction associated with the mechanical consolidation of gouge. J Geophys Res: Solid Earth 103:27239–27256. https://doi.org/10.1029/98JB02639

Naumann M, Hunsche U, Schulze O (2007) Experimental investigations on anisotropy in dilatancy, failure and creep of Opalinus Clay. Phys Chem Earth, Parts a/b/c 32:889–895. https://doi.org/10.1016/j.pce.2005.04.006

Nicolas A, Fortin J, Regnet JB, Dimanov A, Guéguen Y (2016) Brittle and semi-brittle behaviours of a carbonate rock: influence of water and temperature. Geophys J Int 206:438–456. https://doi.org/10.1093/gji/ggw154

Nicolas A et al (2017) Brittle and semibrittle creep of Tavel limestone deformed at room temperature. J Geophys Res: Solid Earth 122:4436–4459. https://doi.org/10.1002/2016JB013557

Niemeijer AR, Spiers CJ (2006) Velocity dependence of strength and healing behaviour in simulated phyllosilicate-bearing fault gouge. Tectonophysics 427:231–253. https://doi.org/10.1016/j.tecto.2006.03.048

Niemeijer A, Marone C, Elsworth D (2008) Healing of simulated fault gouges aided by pressure solution: results from rock analogue experiments. J Geophys Res: Solid Earth. https://doi.org/10.1029/2007JB005376

Niemeijer A, Marone C, Elsworth D (2010) Fabric induced weakness of tectonic faults. Geophys Res Lett. https://doi.org/10.1029/2009GL041689

Nüesch R (1991) Das mechanische Verhalten von Opalinuston. Diss, Switzerland: ETH Zurich 9349

Nussbaum C, Bossart P, Amann F, Aubourg C (2011) Analysis of tectonic structures and excavation induced fractures in the Opalinus Clay, Mont Terri underground rock laboratory (Switzerland). Swiss J Geosci 104:187. https://doi.org/10.1007/s00015-011-0070-4

Nussbaum C, Kloppenburg A, Caër T, Bossart P (2017) Tectonic evolution around the Mont Terri rock laboratory, northwestern Swiss Jura: constraints from kinematic forward modelling. Swiss J Geosci 110:39–66. https://doi.org/10.1007/s00015-016-0248-x

Nygård R, Gutierrez M, Bratli RK, Høeg K (2006) Brittle–ductile transition, shear failure and leakage in shales and mudrocks. Mar Petrol Geol 23:201–212. https://doi.org/10.1016/j.marpetgeo.2005.10.001

Orellana LF, Scuderi MM, Collettini C, Violay M (2018a) Do scaly clays control seismicity on faulted shale rocks? Earth Planet Sc Lett 488:59–67. https://doi.org/10.1016/j.epsl.2018.01.027

Orellana LF, Scuderi MM, Collettini C, Violay M (2018b) Frictional properties of Opalinus Clay: implications for nuclear waste storage. J Geophys Res: Solid Earth 123:157–175. https://doi.org/10.1002/2017jb014931

Orellana LF, Giorgetti C, Violay M (2019) Contrasting mechanical and hydraulic properties of wet and dry fault zones in a proposed shale-hosted nuclear waste repository. Geophys Res Lett 46:1357–1366. https://doi.org/10.1029/2018gl080384

Orellana LF, Giorgetti C, Violay M (2020) Fault creep behavior and the frictional response of the Opalinus Clay formation. In: AGU Fall Meeting Abstracts, 2020. pp MR007–0012

Ortiz L, Volckaert G, Mallants D (2002) Gas generation and migration in Boom Clay, a potential host rock formation for nuclear waste storage. Eng Geol 64:287–296

Paterson MS, Wong T-F (2005) Experimental rock deformation-the brittle field. Springer, Heidelberg, p 348

Pearson FJ et al. (2003) Mont Terri project: geochemistry of water in the opalinus clay formation at the Mont Terri rock laboratory. Reports of the Federal Office for Water and Geology (FOWG) Geology Series No. 5

Popp T, Salzer K (2007) Anisotropy of seismic and mechanical properties of Opalinus clay during triaxial deformation in a multi-anvil apparatus. Phys Chem Earth 32:879–888. https://doi.org/10.1016/j.pce.2006.04.022

Renard F, Beauprêtre S, Voisin C, Zigone D, Candela T, Dysthe DK, Gratier J-P (2012) Strength evolution of a reactive frictional interface is controlled by the dynamics of contacts and chemical effects. Earth Planet Sc Lett 341–344:20–34. https://doi.org/10.1016/j.epsl.2012.04.048

Renner J, Hettkamp T, Rummel F (2000) Rock Mechanical characterization of an argillaceous host rock of a potential radioactive waste repository. Rock Mech Rock Eng 33:153–178. https://doi.org/10.1007/s006030070005

Renner J, Evans B, Siddiqi G (2002) Dislocation creep of calcite. J Geophys Res: Solid Earth 107:ECV 6-1-ECV 6-16. https://doi.org/10.1029/2001JB001680

Rinaldi AP, Urpi L (2020) Fault reactivation induced by tunneling activity in clay material: hints from numerical modeling. Tunn Undergr Space Technol 102:103453. https://doi.org/10.1016/j.tust.2020.103453

Roscoe KH, Burland J (1968) On the generalized stress-strain behavior of wet clays

Ross ZE, Meier M-A, Hauksson E (2018) P wave arrival picking and first-motion polarity determination with deep learning. J Geophys Res: Solid Earth 123:5120–5129. https://doi.org/10.1029/2017JB015251

Ruggieri R et al (2021) The role of shale content and pore-water saturation on frictional properties of simulated carbonate faults. Tectonophysics 807:228811. https://doi.org/10.1016/j.tecto.2021.228811

Ruina A (1983) Slip instability and state variable friction laws. J Geophys Res Solid Earth 88(B12):10359–10370. https://doi.org/10.1029/JB088iB12p10359

Rummel F, Weber U (1999) Sondierbohrung Benken: felsmechanische laboruntersuchung an bohrkernen. Unpublished Nagra interner Bericht Nagra, Wettingen

Rummel F, Hettkamp T, Weber U (1999) DM Experiment: laboratory experiments for the determination of deformation mechanisms and a constitutive law for time dependent deformation behaviour of the Opalinus Clay. Mont Terri technical note TN 1999-35

Rutqvist J et al (2016) Fault activation and induced seismicity in geological carbon storage – lessons learned from recent modeling studies. J Rock Mech Geotech 8:789–804. https://doi.org/10.1016/j.jrmge.2016.09.001

Rutter EH, Glover CT (2012) The deformation of porous sandstones; are Byerlee friction and the critical state line equivalent? J Struct Geol 44:129–140. https://doi.org/10.1016/j.jsg.2012.08.014

Rutter EH, Hadizadeh J (1991) On the influence of porosity on the low-temperature brittle—ductile transition in siliciclastic rocks. J Struct Geol 13:609–614. https://doi.org/10.1016/0191-8141(91)90047-M

Rutter EH, Mainprice DH (1978) The effect of water on stress relaxation of faulted and unfaulted sandstone. Pure Appl Geophys 116:634–654. https://doi.org/10.1007/BF00876530

Rutter E, Wanten P (2000) Experimental study of the compaction of phyllosilicate-bearing sand at elevated temperature and with controlled pore water pressure. J Sediment Res. https://doi.org/10.1306/2DC40902-0E47-11D7-8643000102C1865D

Rutter EH, Atkinson BK, Mainprice DH (1978) On the use of the stress relaxation testing method in studies of the mechanical behaviour of geological materials. Geophys J Int 55:155–170. https://doi.org/10.1111/j.1365-246X.1978.tb04754.x

Saffer DM, Marone C (2003) Comparison of smectite- and illite-rich gouge frictional properties: application to the updip limit of the seismogenic zone along subduction megathrusts. Earth Planet Sc Lett 215:219–235. https://doi.org/10.1016/s0012-821x(03)00424-2

Schleicher AM, van der Pluijm BA, Warr LN (2010) Nanocoatings of clay and creep of the San Andreas fault at Parkfield, California. Geology 38:667–670. https://doi.org/10.1130/G31091.1

Schmid SM (1976) Rheological evidence for changes in the deformation mechanism of Solenhofen limestone towards low stresses. Tectonophysics 31:T21–T28. https://doi.org/10.1016/0040-1951(76)90160-8

Schofield A, Wroth C (1968) Critical State Soil Mechanics.

Schuster K, Amann F, Yong S, Bossart P, Connolly P (2017) High-resolution mini-seismic methods applied in the Mont Terri rock laboratory (Switzerland). Swiss J Geosci 110:213–231. https://doi.org/10.1007/s00015-016-0241-4

Schuster V, Rybacki E, Bonnelye A, Herrmann J, Schleicher AM, Dresen G (2021) Experimental deformation of Opalinus Clay at elevated temperature and pressure conditions:

mechanical properties and the influence of rock fabric. Rock Mech Rock Eng 54:4009–4039. https://doi.org/10.1007/s00603-021-02474-3

Schutjens PMTM (1991) Experimental compaction of quartz sand at low effective stress and temperature conditions. J Geol Soc 148:527–539. https://doi.org/10.1144/gsjgs.148.3.0527

Scott TE, Nielsen KC (1991a) The effects of porosity on fault reactivation in sandstones. J Geophys Res 96:2353–2362

Scott TE, Nielsen KC (1991b) The effects of porosity on the brittle-ductile transition in sandstones. J Geophys Res: Solid Earth 96:405–414. https://doi.org/10.1029/90JB02069

Sibson RH (1985) A note on fault reactivation. J Struct Geol 7:751–754. https://doi.org/10.1016/0191-8141(85)90150-6

Siegesmund S, Popp T, Kaufhold A, Dohrmann R, Grasle W, Hinkes R, Schulte-Kortnack D (2014) Seismic and mechanical properties of Opalinus Clay: comparison between sandy and shaly facies from Mont Terri (Switzerland). Environ Earth Sci 71:3737–3749. https://doi.org/10.1007/s12665-013-2768-2

Soe AKK, Osada M, Takahashi M, Sasaki T (2009) Characterization of drying-induced deformation behaviour of Opalinus Clay and tuff in no-stress regime. Environ Geol 58:1215–1225. https://doi.org/10.1007/s00254-008-1616-2

Stanchits S, Mayr S, Shapiro S, Dresen G (2011) Fracturing of porous rock induced by fluid injection. Tectonophysics 503:129–145. https://doi.org/10.1016/j.tecto.2010.09.022

Tembe S, Lockner DA, Wong T-F (2010) Effect of clay content and mineralogy on frictional sliding behavior of simulated gouges: binary and ternary mixtures of quartz, illite, and montmorillonite. J Geophys Res: Solid Earth. https://doi.org/10.1029/2009jb006383

Tesei T, Collettini C, Carpenter BM, Viti C, Marone C (2012) Frictional strength and healing behavior of phyllosilicate-rich faults. J Geophys Res: Solid Earth. https://doi.org/10.1029/2012JB009204

Thury MF, Bossart PJ (1999) Mont Terri rock laboratory: results of the hydrogeological, geochemical and geotechnical experiments performed in 1996 and 1997. vol Geologischer Bericht Nr. 23. Landeshydrologie und-geologie

Tsang CF, Barnichon JD, Birkholzer J, Li XL, Liu HH, Sillen X (2012) Coupled thermo-hydro-mechanical processes in the near field of a high-level radioactive waste repository in clay formations. Int J Rock Mech Min 49:31–44. https://doi.org/10.1016/j.ijrmms.2011.09.015

Urpi L, Rinaldi AP, Rutqvist J, Wiemer S (2019) Fault stability perturbation by thermal pressurization and stress transfer around a deep geological repository in a clay formation. J Geophys Res: Solid Earth 124:8506–8518. https://doi.org/10.1029/2019JB017694

Vannucchi P, Maltman A, Bettelli G, Clennell B (2003) On the nature of scaly fabric and scaly clay. J Struct Geol 25:673–688. https://doi.org/10.1016/S0191-8141(02)00066-4

Vrolijk PJ, Urai JL, Kettermann M (2016) Clay smear: review of mechanisms and applications. J Struct Geol 86:95–152. https://doi.org/10.1016/j.jsg.2015.09.006

Wenk HR, Voltolini M, Mazurek M, Van Loon LR, Vinsot A (2008) Preferred orientations and anisotropy in shales: Callovo-Oxfordian shale (France) and Opalinus Clay (Switzerland). Clay Clay Miner 56:285–306. https://doi.org/10.1346/Ccmn.2008.0560301

Wenning QC et al (2021) Shale fault zone structure and stress dependent anisotropic permeability and seismic velocity properties (Opalinus Clay, Switzerland). J Struct Geol 144:104273. https://doi.org/10.1016/j.jsg.2020.104273

Wild KM, Amann F (2018) Experimental study of the hydro-mechanical response of Opalinus Clay - Part 1: pore pressure response and effective geomechanical properties under consideration of confinement and anisotropy. Eng Geol 237:32–41. https://doi.org/10.1016/j.enggeo.2018.02.012

Wild KM, Wymann LP, Zimmer S, Thoeny R, Amann F (2015) Water retention characteristics and state-dependent mechanical and petro-physical properties of a clay shale. Rock Mech Rock Eng 48:427–439. https://doi.org/10.1007/s00603-014-0565-1

Winhausen L et al (2020) A comparative study on methods for determining the hydraulic properties of a clay shale. Geophys J Int. https://doi.org/10.1093/gji/ggaa532

Winhausen L, Khaledi K, Jalali M, Urai JL, Amann F (2022) Failure mode transition in Opalinus Clay: a hydro-mechanical and microstructural perspective. Solid Earth 13:901–915. https://doi.org/10.5194/se-13-901-2022

Wong T-f, Baud P (2012) The brittle-ductile transition in porous rock: a review. J Struct Geol 44:25–53. https://doi.org/10.1016/j.jsg.2012.07.010

Wong T-f, David C, Zhu W (1997) The transition from brittle faulting to cataclastic flow in porous sandstones: mechanical deformation. J Geophys Res: Solid Earth 102:3009–3025. https://doi.org/10.1029/96JB03281

Wood DM (1990) Soil behaviour and critical state soil mechanics. Cambridge University Press, Cambridge. https://doi.org/10.1017/CBO9781139878272

Yasuhara H, Marone C, Elsworth D (2005) Fault zone restrengthening and frictional healing: the role of pressure solution. J Geophys Res: Solid Earth. https://doi.org/10.1029/2004JB003327

Zhang C-L, Laurich B (2019) Mechanical behavior of sandy facies of Opalinus Clay under different load conditions. J Rock Mech Geotech. https://doi.org/10.1016/j.jrmge.2019.09.005

Zhang X, Spiers CJ (2005) Compaction of granular calcite by pressure solution at room temperature and effects of pore fluid chemistry. Int J Rock Mech Min 42:950–960. https://doi.org/10.1016/j.ijrmms.2005.05.017

Zhang X, Spiers CJ, Peach CJ (2010) Compaction creep of wet granular calcite by pressure solution at 28°C to 150°C. J Geophys Res: Solid Earth. https://doi.org/10.1029/2008JB005853

Zoback MD (2007) Reservoir geomechanics. Cambridge University Press, Cambridge. https://doi.org/10.1017/CBO9780511586477

Zoback MD, Gorelick SM (2012) Earthquake triggering and large-scale geologic storage of carbon dioxide. Proc Natl Acad Sci 109:10164. https://doi.org/10.1073/pnas.1202473109

Zoback MD, Kohli AH, Das I, McClure MW (2012) The Importance of slow slip on faults during hydraulic fracturing stimulation of shale gas reservoirs. Paper presented at the SPE Americas Unconventional Resources Conference, Pittsburgh, Pennsylvania USA, June 2012. https://doi.org/10.2118/155476-MS